

pubs.acs.org/JPCC Article

Sensitive T2 MRI Contrast Agents from the Rational Design of Iron Oxide Nanoparticle Surface Coatings

Published as part of The Journal of Physical Chemistry virtual special issue "Horst Weller Festschrift".

Minjung Cho, Jake Villanova, Dylan M. Ines, Jingge Chen, Seung Soo Lee, Zhen Xiao, Xiaoting Guo, Joshua A. Dunn, Deanna D. Stueber, Paolo Decuzzi, and Vicki L. Colvin*



Cite This: J. Phys. Chem. C 2023, 127, 1057-1070



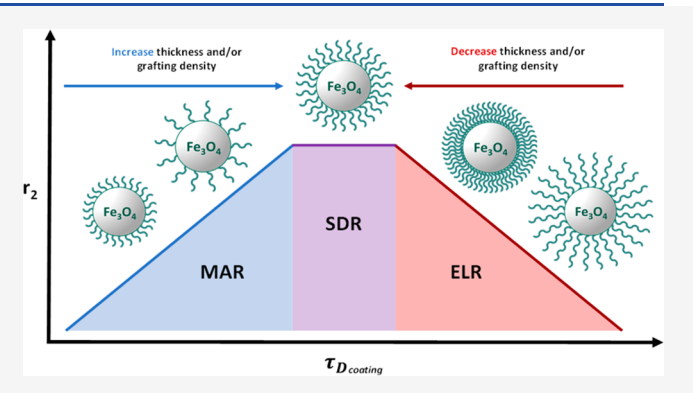
ACCESS

III Metrics & More

Article Recommendations

s Supporting Information

ABSTRACT: Iron oxide nanoparticles are an FDA-approved and gadolinium-free alternative to conventional magnetic resonance imaging (MRI) contrast agents. While their magnetic cores are responsible for T_2 contrast, the nonmagnetic polymers at the particle interfaces can affect the diffusion of bulk water near the particles. We show here how this interaction can alter the relaxation dynamics of water protons and, consequently, the nanoparticle's contrast performance. Libraries of iron oxide nanocrystals of different core diameters and surface coatings can form biocompatible, non-cytotoxic, and colloidally stable suspensions with excellent MRI properties. Both the grafting density and thickness of polymer coatings influence the amount of time water protons spend around a nanoparticle and thus their contrast agent



performance. Characterization of the diameter-dependent contrast performance of these materials revealed that nanoparticles with dense, hydrophilic polymer coatings reached the static dephasing regime, and optimal T_2 relaxivity, at smaller dimensions than other systems. We rationalized that such coatings offered a slow compartment for water diffusion near the magnetic particle, resulting in an effective diffusion constant lower than bulk water. By manipulating the surface coating and core diameter together, we could generate a material with one of the largest T_2 relaxivities ever reported (510 mM⁻¹ s⁻¹) for an isolated nanocrystal. This conceptual framework can explain the complex structure—performance trends of this class of T_2 contrast agents and those already reported in the existing literature. Water diffusion at iron oxide nanocrystals (IONCs) interfaces is an essential consideration in designing sensitive and possibly responsive T_2 MRI contrast agents.

1. INTRODUCTION

Iron oxide nanocrystals (IONCs) have attracted considerable interest as gadolinium-free MRI contrast agents. 1-3 These materials generate localized inhomogeneous magnetic fields during MRI leading to an acceleration in the transverse water 1 H relaxation time (T_{2}) near their surface, resulting in a negative, or dark, contrast. Their favorable biocompatibility, hepatobiliary biodistribution, and clearance mechanisms have made them the only gadolinium-free MRI contrast agent approved by the U.S. Food and Drug Administration (FDA) for clinical use.1 Commercial IONCs such as ferumoxytol (Feraheme) have been used for diverse applications, including tumor imaging (e.g., liver, spleen, lymph nodes, brain), stem cell tracking, angiography, and perfusion imaging.⁴ With their increased relevance has come an interest in using MRI contrast agents as a signal for the presence or absence of key biomarkers. Molecular MRI using nanoparticles has generally relied on stimuli-responsive clustering phenomena; while successful at creating MRI contrast, the research is not easily translated given the persistence and toxicity of larger aggregates. S-19 Alternative strategies that modulate contrast agent signal based on changes to their surface coatings could provide another route for molecular imaging. Such an advance requires a detailed elaboration of the role of the nonmagnetic surface coating in IONC design. 2-4,20,21

Models describing these materials detail how the varying magnetic fields present near a nanocrystal surface perturb the water proton relaxation processes. This results in a spread of proton Larmor frequencies, $\Delta \omega$, and how much this affects MRI contrast will depend on the amount of time water spends in the spin-perturbed region, $\tau_{\rm D}$. When water spends the

Received: July 29, 2022 Revised: November 8, 2022 Published: January 6, 2023





entirety of the MRI measurement time diffusing through the inhomogeneous magnetic fields near nanocrystals, a condition broadly referred to as the static dephasing regime (SDR), then the contrast agent will have its largest signal. ^{3,24,25} This optimal time scale is typically reached through careful manipulation of the iron oxide dimension. ^{22,23,26-28} Weller et al. showed how as aggregated IONCs increased in diameter their performance first increased and then decreased, and identified a SDR for aggregates with hydrodynamic diameters of about 60-120 nm. ²⁹ The ultimate performance of iron oxide nanoparticles optimized for SDR will depend on the core crystallinity, composition, and shape as these factors affect the inhomogeneous magnetic field experienced by freely diffusing water. ³⁰⁻⁴⁰

Relatively less attention has centered on how the nonmagnetic elements of T2 contrast agents affect their imaging performance. IONC coatings are primarily selected for their ability to prevent aggregation of magnetic particles in relevant biological media and secondarily for appropriate pharmacokinetics, biodistribution, and biocompatibility.^{2,3} However, these coatings could be expected to alter the time water protons spend in the inhomogeneous magnetic field near particles and thus should play some role in defining T2 contrast. Studies of T₂ nanocrystal contrast agents have found that contrast performance can be affected by surface coatings. 36,41-56 Water impermeable coatings, for example, are detrimental to contrast as they exclude water from the near-particle region, causing as much as a 70-90% decrease in performance with increasing thickness. 50,51 Trends for water-permeable coatings are more difficult to discern. A "slow compartment" model has been suggested to account for water permeation into surface coatings which leads to an effective water diffusion constant less than bulk water. 53 However, whether slowing water down around an IONC is beneficial for T2 contrast is not immediately apparent as apparently contradictory trends have been reported with respect to coating thickness and molecular weight.53

Here iron oxide nanocrystals with different polymeric surface coatings are used to clarify how the surface coating of an IONC may change its relaxivity. These diametercontrolled, hydrophobic nanocrystals (4-33 nm) are monodisperse and amenable to several distinct surface coating strategies. The resulting materials have good biocompatibility with excellent colloidal and relaxometric stability over a range of physiologically relevant conditions. The systems have sizeand surface-dependent T₂ relaxivity trends that together can be rationalized by a slow compartment model that also considers the core diameter dependence. For T2 contrast agents small enough to be in the motional averaging regime (MAR), coatings that slow water protons lead to an increase in relaxivity. For larger core materials already optimized for SDR, water permeable polymers have the opposite effect and slow water down so much that the contrast is suppressed, a limit referred to as the echo limited regime (ELR). Materials optimized with both their surface and diameter exhibit performance greater than commercial IONCs (>200 mM⁻¹ s⁻¹) and similar IONCs reported in the literature (>385 mM⁻¹ s^{-1}). $^{4,27,28,30-38,57-59}$ Water permeable coatings also affect the size-dependent trends in these systems by shifting SDR, where optimal performance is observed, to smaller core diameters. The accompanying description of these trends showcases the essential role that surface coatings play in CA performance and helps rationalize the existing reports of surface-dependent effects seen in this work as well as the broader literature.

2. METHODS

2.1. Materials. Iron(III) oxide (FeO(OH), hydrated, catalyst grade, 30-50 mesh), 1-octadecene (1-ODE, technical grade 90%), oleic acid (OA, technical grade 90%), octylamine (99%), 2-acrylamido-2-methylpropanesulfonic acid copolymer (PAMPS), poly(acrylic acid) (PAA, $M_w = 1800$ Da), lauryl acrylate (LA, technical grade 90%), poly(maleic anhydride-alt-1-octadecene) (PMAO, $M_w = 30,000-50,000$), calcium sulfate (≥97.0%), 1% penicillin-streptomycin (PS), Dulbecco's modified Eagle's medium (DMEM, ATTC, Mannassa, VS), fetal bovine serum (FBS), and trypsin-EDTA were obtained from Sigma-Aldrich. Acetone (99.5%), nitric acid (HNO₃, 70%), diethyl ether (DEE, certified ACS), ethanol (99.8%), methanol (certified ACS), dimethylformamide (DMF, 99.8%), hexanes (98.5%), 1-ethyl-3-[3-(dimethylamino)propyl] carbodiimide hydrochloride (EDC), sodium bicarbonate (99.7%), and hydrogen peroxide (H2O2, 30%) were obtained from Fisher Scientific. Methyl ether poly(ethylene glycol) amine (mPEG-NH₂) ($M_{\rm w}$ = 2000 Da) was obtained from Laysan Bio. Human dermal fibroblasts (HDF) were obtained from Cambrex. CellTiter 96 Aqueous One solution Cell Proliferation Assay (MTS assay) was obtained from Promega.

2.2. Synthesis of Size-Controlled Iron Oxide Nanocrystals. Hydrophobic iron oxide nanocrystals (IONCs) were synthesized by a modified procedure reported previously by our group. 60 Iron(III) oxide (FeO(OH), 0.178 g), oleic acid (OA, 2.26 g), and 1-octadecene (1-ODE, 5 g) are mixed in a 100 mL three neck flask and heated to 120 °C for 2 h to remove residual water. The solution is then heated to 240 °C for 30 min to generate iron oleate, which is a precursor to nanocrystal formation. After further heating to 320 °C for 2 h under inert conditions (N2), the precursor decomposes yielding IONCs. To purify the resulting black colloidal nanocrystal sample, 20 mL of methanol and 20 mL of acetone are added to 5 mL of sample and centrifuged at 4150 rpm for 30 min. Treatment with hexanes allows this precipitate to be dissolved, and the process of centrifugation and resuspension is repeated six times. The final solution containing 10 nm IONCs is stored in hexanes. For 16 nm IONCs, the molar ratio between FeO(OH) and oleic acid is changed from 1:4 to 1:5 with all other conditions remaining the same. For 4 nm IONCs, the above prepared iron oleate (0.15 mmol, 0.09 g) and oleic acid (0.3 mmol, 0.08 g) are mixed with 5 g of 1-ODE at 320 °C for 0.5 h under inert conditions (N2). For 33 nm IONCs, a mixture of FeO(OH) (50 mmol, 4.5 g), oleic acid (200 mmol, 56 g), and 1-ODE (40 mmol, 10 g) are heated to 240 °C for 2 h and then 320 °C for 12 h.

2.3. Oleic Acid Bilayer Coating. An oleic acid bilayer serves as a suitable coating for these materials and is generated following a previously published procedure. Briefly, oleic acid $(0.95-9.5~\mu\text{M})$ is mixed with 1 mL of nanocrystal solution dispersed in ethyl ether $(1,500-4,000~\text{mg}~\text{Fe}~\text{L}^{-1})$. After stirring of the mixture for 24 h, ultrapure water (Millipore, 18.2 M Ω) or 0.1 M sodium bicarbonate (pH 9) solution is added and stirred for an additional 2 h. To facilitate dispersion in water, the sample is probe sonicated (UP 50H, Hielscher Ultrasonics) at a 60% amplitude for 10 min. While stirring, the sample is uncovered for 24 h resulting in the complete evaporation of residual organic solvent. Sample purification is carried out using ultracentrifugation (Optima L-90K ultracentrifuge, Beckman coulter) at 35,000 rpm for 3 h twice, followed by syringe filtration (pore size of 0.45 μ m, Whatman

nylon). Inductively coupled plasma—optical emission spectroscopy (Agilent, ICP-OES) is used to determine the phase transfer yield by the iron concentration of samples before and after phase transfer.

2.4. Octylamine (OA)-Modified Poly(acrylic acid) (PAA-OA) Coating. Octylamine-modified poly(acrylic acid) (PAA-OA) polymer and PAA-OA coated nanocrystals were prepared by a previously published procedure. To generate PAA-OA, PAA (0.6 g, 0.33 mmol) is dissolved in DMF (10 g) and stirred for 10 min. Then, EDC (0.58 g, 3 mmol) is added to PAA/DMF solution, followed by octylamine (0.5 mL, 3 mmol). After stirring overnight, a rotary evaporator (Buchi Rotavapor R-200) is used to remove DMF as the PAA-OA solution is subjected to a vacuum. Finally, a 15 mg mL⁻¹ solution of PAA-OA in 40 mL of chloroform is made.

PAA-OA polymer solutions (1–7 mL) are mixed with 1 mL of nanocrystal solution (typically 1,500–4,000 mg Fe L⁻¹ in chloroform) and stirred for 24 h. Chloroform is allowed to evaporate using air or a vacuum. Sodium bicarbonate (0.1 M, 10 mL) is added, and the resulting suspension is probe sonicated at 60% amplitude for 10 min. Purification relies on ultracentrifugation (40,000 rpm for 3 h, twice) and syringe filtration (0.45 μ m, Whatman nylon) providing a black product that is easily dispersed in ultrapure water (Millipore, 18.2 M Ω). Inductively coupled plasma—optical emission spectroscopy (ICP-OES) is used to determine the phase transfer yield through the measurement of the iron concentration of samples before and after phase transfer.

2.5. Poly(2-acrylamido-2-methylpropanesulfonic acid) (PAMPS)-lauryl Acrylate (LA) (PAMPS-LA) Coating. Poly(2-acrylamido-2-methylpropanesulfonic acid)-lauryl acrylate (PAMPS-LA) is synthesized via copolymerization of 30 g of AMPS (207.23 Da, 0.1447 mol) and 22.5 mL of LA (240.38 Da, 0.0827 mol) in 300 mL of DMF solution. This photoinitiated reaction occurs when exposed to ultraviolet light of 352 nm wavelength. As synthesized PAMPS-LA was used without further purification. The varied ratios of PAMPS-LA polymer per nanocrystal are prepared by adding 1-7 mL (15 mg mL⁻¹ in DMF) to 1 mL of nanocrystal solution (typically 1,500-4,000 mg Fe L⁻¹ in diethyl ether (DEE)). If the mixture is cloudy, more DMF may be added to further solubilize the polymer. After stirring for 24 h, ultrapure Milli-Q water is added (10 mL), the solution is stirred uncovered for 24 h, and the diethyl ether is evaporated. Samples are purified of excess free polymer in solution using ultracentrifugation (40,000 rpm for 3 h, twice) and syringe filtration (0.45 μ m, Whatman, nylon) and redispersed in ultrapure water. Inductively coupled plasma-optical emission spectroscopy (Agilent, ICP-OES) is used to determine the phase transfer yield from the iron concentration of samples before and after phase transfer.

2.6. Poly(maleic anhydride-alt-1-octadecene) (PMAO)-Poly(ethylene glycol) (PEG) Methyl Ethers (mPEG-NH2) (PMAO-PEG) Coating. The method for coating poly(maleic anhydride-alt-1-octadecene-poly(ethylene glycol) (PMAO-PEG) onto nanocrystals is adapted from a previously reported protocol. PMAO ($M_{\rm w}=30-50~{\rm kDa}$) is mixed with mPEG-NH2 ($M_{\rm w}=2~{\rm kDa}$) in chloroform and stirred overnight to make the PMAO-PEG amphiphilic copolymer (molar ratio of PMAO/PEG, 1:5 to 1:30). The varied ratios of PMAO-PEG to nanocrystal are prepared by adding 1–7 mL (20 mg L $^{-1}$) of polymer solutions to 1 mL nanocrystal solutions (typically 1,500–4,000 mg Fe L $^{-1}$ in

chloroform) followed by 24 h of stirring. During this time chloroform is allowed to evaporate using air or a vacuum. After 0.1 M sodium bicarbonate (10 mL) is added, the mixture is probe sonicated at 60% amplitude for 10 min. Purification proceeds using ultracentrifugation (40,000 rpm for 3 h, twice) and syringe filtration (0.45 μ M, Whatman NYL), followed by redispersion of purified product into ultrapure water. Inductively coupled plasma—optical emission spectroscopy (ICP-OES) is used to determine the phase transfer yield by the iron concentration of samples before and after phase transfer.

- 2.7. Transmission Electron Microscopy (TEM). The nanocrystal sample diameter and size variation are determined using a field emission JEOL 2100 transmission electron microscope (TEM) operating at 200 kV with a single tilt holder. Samples are prepared for TEM by evaporating one drop of nanocrystal solution on an ultrathin 400 mesh copper grid (Ted Pella Inc.). Average nanocrystal size and standard deviation are determined using Image-Pro Plus 5.0 (Media Cybernetics, Inc., Silver Spring, MD) image analysis software to detect edges, smooth holes, and determine the diameter for at least 500 nanocrystals per sample. Resultant size distribution histograms are fit with a Gaussian curve to obtain average diameters and distribution width.
- **2.8.** X-ray Diffraction (XRD). The nanocrystal sample crystallinity is determined using a Bruker D8 Discovery 2D X-ray diffractometer operating at 40 mA and 40 kV with a Cu tube (1.5413 Å). A highly concentrated representative nanocrystal sample is drop cast onto a glass slide and allowed to dry. The diffraction pattern is smoothed using Microsoft Excel.
- **2.9. Dynamic Light Scattering (DLS).** The hydrodynamic diameter (nm) and zeta potential (mV) of all synthesized and surface functionalized materials is measured using a ZEN-3600 Zetasizer Nano (Malvern, UK) equipped with a HeNe 633 nm laser. Prior to measurement, surface coated nanocrystal samples in water were purified using a 0.45 μ m nylon syringe filter (Whatman). The recorded hydrodynamic diameters (nm) are the number-average of five measurements for each sample. Size distribution curves were monomodal, and the number-averaged values are an effective representation of our distribution. We had no larger dimensions or sizes present in the number-averaged data from these exact samples; materials made using these synthetic methods have intensity-averaged DLS size distributions consistent with samples that are >99% nonaggregated iron oxide nanocrystals. 61,65,68
- **2.10.** Inductively Coupled Plasma-Optical Emission Spectroscopy (ICP-OES). To measure the concentration of iron, a PerkinElmer ICP-OES equipped with an auto sampler is used. Samples are prepared for ICP-OES analysis by acid digestion using nitric acid (HNO $_3$, 70%) followed by hydrogen peroxide (H $_2$ O $_2$, 30%).
- 2.11. Matrix Assisted Laser Desorption Ionization Time-of-Flight Mass Spectroscopy (MALDI-TOF-MS). To measure the molecular weight of polymers a matrix assisted laser desorption ionization time-of-flight (MALDI-TOF) mass spectrometer (Bruker Autoflex II MALDI-TOF) equipped with a nitrogen laser operated at 337 nm is used. To prepare samples for analysis, 1 μ L of polymer is dissolved in a 4:1 solution of acetonitrile and water with 0.1% (v/v) trifluoroacetic acid. Then, trace α -cyano-4-hydroxycinnamic acid matrix is dissolved in a 4:1 solution of acetonitrile and water with 0.1% (v/v) trifluoroacetic acid. After evaporation of 1 μ L

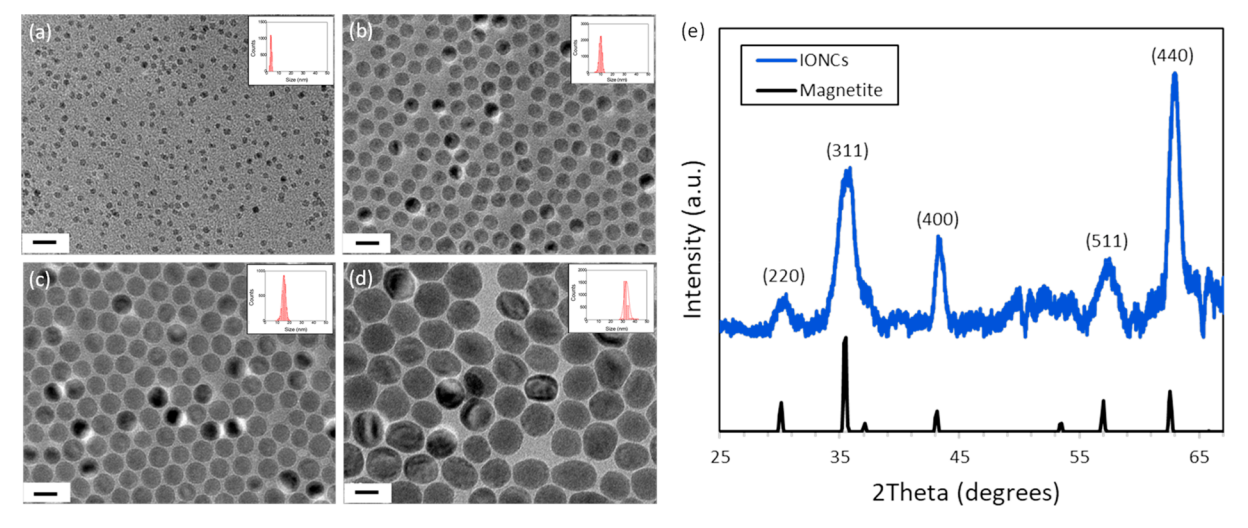


Figure 1. Transmission electron microscopy (TEM) images with inset size distribution histograms of as-synthesized, monodisperse iron oxide nanocrystals of varying core diameter (a–d). Core diameters are (a) 4.0 ± 0.6 , (b) 10.2 ± 0.7 , (c) 16.0 ± 1.4 , and (d) 33.1 ± 2.5 nm. Scale bars are 20 nm. (e) XRD pattern for a representative sample of iron oxide nanocrystals. The sample diffraction pattern (blue) is consistent with a standard pattern for magnetite (Fe₃O₄; black).

of the sample solution on the plate, another 1 μ L of matrix solution is overlaid on sample spot and allowed to dry.

2.12. Vibrating Sample Magnetometry (VSM). Sample saturation magnetization was measured using a Lake Shore 7400 Series vibrating sample magnometer at 300 K. Prior to analysis, solid samples obtained from dried nanocrystal solutions were mixed with a nonmagnetic matrix. Solid samples were prepared by mixing 100 μ L of nanocrystal solution (1000 ppm Fe) with 10 mg of calcium sulfate and drying at 60 °C. The hysteresis loop was measured at room temperature between 10,000 and -10,000 Oe. Representative 5, 8, 13, 19, and 31 nm IONCs were synthesized as previously reported and used for these experiments. The mass saturation magnetization $(M_s, \text{ emu g}^{-1})$ of these samples at 10,000 Oe were plotted against their diameters (nm). These data were fit logarithmically and used as a standard curve to find the saturation magnetization for the 4, 10, 16, and 33 nm IONCs used in all previous experiments; this approach could introduce some error into our measurements if there are variations which may be amplified as we rely on scaling that is sensitive to the square of M_v . We also use the M_v values at 1 T to normalize the r_2 results at 1.5 T. The magnetization curves show that at 1 T samples are nearly fully magnetized, but this could also introduce some error. For all conversions between M_s and volumic saturation magnetization ($M_{\rm v}$, $10^{\rm 5}~{\rm A~m^{-1}}$), $\rho_{\rm magnetite}$ = 5.18×10^6 g m⁻³ is used with the conversion factor from emu to A m^2 (1 emu = 10^3 A m^2).

2.13. Relaxivity Measurements. Various concentrations of nanocrystals are prepared by dilution using a 0.22 μ m syringe filter from stock aqueous solutions of nanocrystals with different coatings for MR relaxivity measurement. The concentration of nanocrystals in the stock is determined as described below. An MR relaxometer (NMR analyzer, mq60, Bruker, 1.41 T) is used to determine the T_2 of each sample over a range of concentrations. T_2 measurements are obtained via monoexponential decay curves generated using a Carr–Purcell–Meiboom–Gill (CPMG) echo train sequence with a 20 s recycle delay, 2 s echo time (τ = 1 s), and 500 data points at 37 C. 62,63 The r_2 of each sample is determined from the slope of $1/T_2$ plotted as a function of Fe concentration. Using

eq 3, $C/D_{\rm eff}$ and therefore $D_{\rm eff}$ can be approximated from the slope of the line generated from a plot of $r_2/M_{\rm v}^2$ as a function of d^2 for each coating using samples in MAR. $\nu_{\rm mat}$ is the molar volume of magnetic ions in the material defined as the ratio of the volume fraction of nanocrystals in solution (f) to the atomic concentration of magnetic ions [M] ($v_{\rm mat} = f/[M]$; $\nu_{\rm magnetite} = 0.2314~{\rm kg~mol}^{-1}/3(5180~{\rm kg~m}^{-3}) = 1.49 \times 10^{-5}~{\rm m}^3~{\rm mol}^{-1}$),

2.14. In Vitro MRI Phantoms. In vitro T_2 weighted MR phantom studies were performed in a clinical 3 T scanner (Philips Ingenia) using a turbo spin echo (TSE) sequence with TR = 2500 ms, TE = 100 ms and a slice thickness of 400 mm. Images are collected from IONC samples with different concentrations, core sizes, and coating.

2.15. Cell Culture and MTS Assay. Human dermal fibroblasts (HDF, Cambrex) are cultured in Dulbecco's modified Eagle's medium (DMEM, ATCC, Manassas, VS) with 10% fetal bovine serum (FBS) and 1% penicillinstreptomycin (PS). HDF cells are floated by trypsin-EDTA and resuspended in media (DMEM with 10% FBS and 1% PS) solution for the passaging.

A standard colorimetric MTS assay (CellTiter 96, Promega) is used to determine the nanocrystal cytotoxicity. HDF cells are grown in 96 well culture plates with over 80% confluency. Each set is prepared with different concentrations of nanocrystal solutions. One set is treated as a blank (no nanocrystals), and the last set is used for the untreated control (ethanol). Cells are incubated with select aqueous nanocrystal solution for 24 h. This solution is then suctioned out and replaced with 100 μ L of fresh media (DMEM with FBS 10% and 1% PS) solution and 20 μL of MTS agent in each well. After incubation for 1 h at 37 °C and 5% CO₂, the solution absorbance at 490 nm is measured via a plate reader (Spectra Max, M2, Molecular devices). All experiments are done in triplicate. The LD₅₀ for each sample, which gives the dose required for 50% cell death, is calculated by the percentage of cell viability.

2.16. Total Organic Carbon (TOC) Analysis. A Shimadzu TOC-L is used to measure the carbon concentration for surface functionalized nanocrystals in water. Samples are

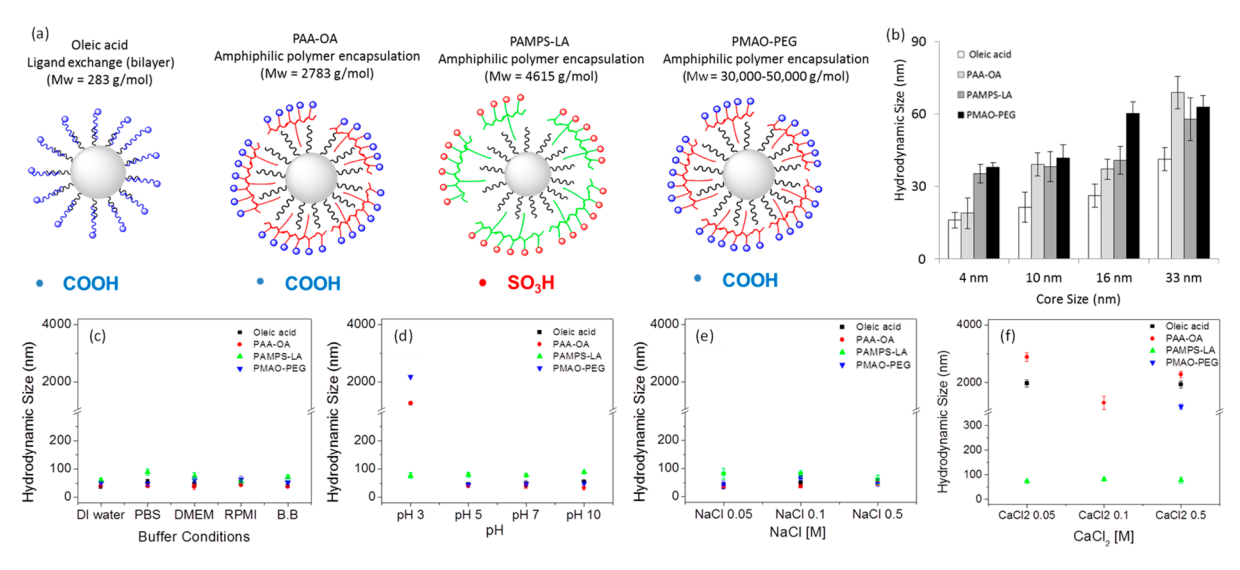


Figure 2. (a) Schematic depiction of iron oxide nanocrystals with various encapsulation phase transfer agents (oleic acid bilayer, PAA-OA, PAMPS-LA, and PMAO-PEG). (b) The hydrodynamic diameter (HD) and of 4, 10, 16, and 33 nm iron oxide nanocrystals with different surface coatings (oleic acid bilayer, PAA-OA, PAMPS-LA, and PMAO-PEG). Hydrodynamic sizes of iron oxide nanocrystals (10 nm) dispersed in different (c) buffer solutions (distilled ionized water (DI water), phosphate buffer saline (PBS), Dulbecco's Modified Eagle's Medium (DMEM) and Roswell Park Memorial Institute medium (RPMI), and borate buffer (B.B)), (d) pH 3–10, (e) NaCl 0.05–0.5 M, and (f) CaCl₂ 0.05–0.5 M.

Table 1. T_2 Relaxivity (r_2) and Hydrodynamic Diameter (HD) of Iron Oxide Nanocrystals with Different Sizes and Phase Transfer Coatings

core size/coating	oleic acid bilayer		PAA-OA		PAMPS-LA		PMAO-PEG	
Iron Oxide Sample	HD (nm)	$r_2~(\mathrm{mM}^{-1}\mathrm{s}^{-1})$	HD (nm)	$r_2~(\mathrm{mM}^{-1}\mathrm{s}^{-1})$	HD (nm)	$r_2~(\mathrm{mM}^{-1}\mathrm{s}^{-1})$	HD (nm)	$r_2 \left({ m mM}^{-1} { m s}^{-1} \right)$
4 nm	16.0±3.1	11.1±3.1	18.9±6.4	81.9 <u>±</u> 6.4	35.3±3.9	108.7±3.9	37.8 ± 2.1	126.6±3.1
10 nm	21.3 ± 6.2	50.5 ± 2.8	39.1 ± 4.9	158.9 ± 5.9	38.2 ± 6.2	152.4 ± 7.2	41.7 ± 5.6	201.1 ± 5.7
16 nm	26.2 <u>±</u> 4.7	159.8 ± 10.7	37.1 ± 4.2	327.7 ± 12.5	40.8 ± 5.7	385.2 ± 10.1	60.2 ± 4.7	260.4 ± 12.9
33 nm	41.3±4.8	510.3±18.8	68.8 ± 6.8	301.2 ± 10.4	57.8±8.8	355.1±6.7	62.9 ± 4.8	339.9 ± 8.3

prepared by diluting 1 mL of the stock nanocrystal solution to 8.5 mL with Milli-Q water. Each sample is run on a total nonpurgeable organic carbon (NPOC) assay with triplicate 50 μ L injections. A standard calibration curve is made based on a range of carbon concentrations (0.5–60 ppm) prepared using a TOC standard solution (Sigma-Adrich) ($R^2 = 0.998$).

2.17. Grafting Density Calculation. Grafting density (σ) is calculated from TOC data using the equation below:⁶⁴

$$\sigma = \frac{[C]^* M_{\rm n}}{M_{\rm p}^* C_{\rm n}^* [NP]^* (4\pi r_{\rm core}^2)}$$
(1)

The nonpurgeable organic carbon concentration ([C]) from the TOC analysis is converted from mg L⁻¹ (ppm) to mol L⁻¹ (M) by using molar mass of carbon (12,010 mg mol⁻¹). To determine the number of polymer molecules grafted on the nanocrystal surface (σ), the carbon concentration is multiplied by the molecular weight of the monomer ($M_{\rm n}$) and divided by the polymer molecular weight ($M_{\rm p}$), number of carbons per monomer ($C_{\rm n}$), molar concentration of nanocrystals ([NP]), and surface area of the nanocrystal ($4\pi r^2_{\rm core}$).

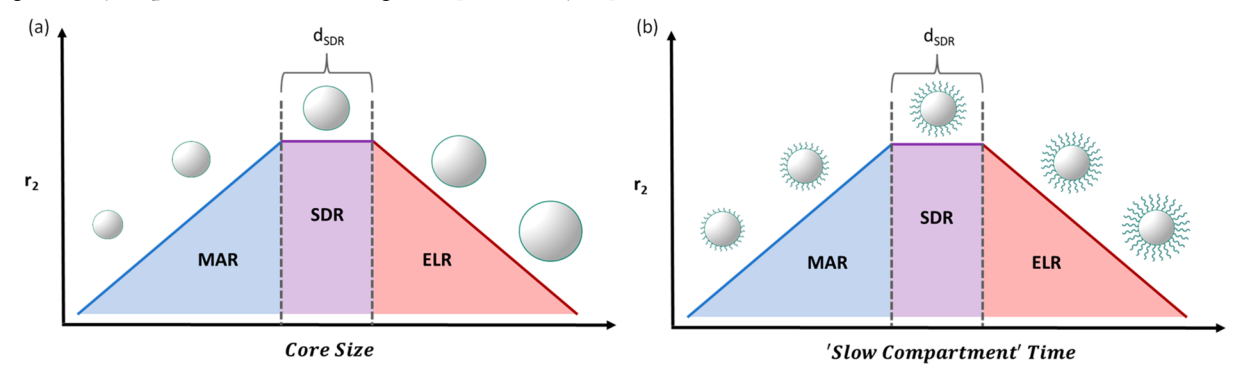
3. RESULTS AND DISCUSSION

3.1. Synthesis, Diameter Control, and Phase Transfer of Monodisperse Iron Oxide Nanocrystals. Iron oxide nanocrystals (IONCs) are prepared via thermal decomposition of iron precursors in the presence of oleic acid at high temperature (320 °C). Transmission electron microscopy

(TEM) images indicate as synthesized IONCs are monodisperse and quasi-spherical with diameters of approximately 4, 10, 16, and 33 nm (Figure 1a–d). Diameter control is achieved by either changing the reaction time or the molar ratio of iron precursor to oleic acid. Because of Ostwald ripening, the latter is generally a preferred approach as nanocrystal uniformity diminishes after several hours. As has been reported before, IONCs are crystalline and nonaggregated with a structure consistent with the magnetite (Fe₃O₄) phase of iron oxide (Figure 1e). ^{65,66}

The hydrophobic nanocrystals are formed with oleic acid bound to their surfaces, and subsequently transferred into aqueous solution via either encapsulation or ligand exchange methods.^{67,68} Encapsulation results in bilayer stabilized IONCs and utilizes a phase transfer process facilitated by the addition of excess oleic acid or amphiphilic polymers like octylaminemodified poly(acrylic acid) (PAA-OA), poly(2-acrylamido-2methylpropanesulfonic acid)-lauryl acrylate (PAMPS-LA), and poly(maleic anhydride-alt-1-octadecene)-poly(ethylene glycol) (PMAO-PEG) (Figures 2a and S1). Alternatively, as synthesized IONCs can also have their original oleic acid removed and replaced by poly(ethylene glycol) (PEG; 0.2, 1, and 10 kDa), poly(vinylpyrrolidone) (PVP; 1 kDa), and poly(acrylic acid) (PAA; 15 kDa). These phase transfer processes are efficient with typical yields of 70%. Either method provides IONCs in a colloidally stable, clear, and brownish black colloidal suspension. Dynamic light scattering (DLS) reveals that the hydrodynamic diameter (HD) of the

Scheme 1. Schematic Representations of the Effect of (a) Magnetic Nanocrystal Core Size and (b) Water Diffusion Time through Its Hydrophilic Surface Coating on T_2 Relaxivity $(r_2)^a$



"Notice, because of the "slow compartment" effect on the diffusion of water, the core size needed to achieve SDR (d_{SDR}) is smaller for magnetic nanocrystals with a hydrophilic surface coating.

nanocrystals increases with core size and the molecular weight of the coating; for these samples HD is always well under 100 nm (Figure 2b, Tables 1 and S1). A consideration of the core dimensions, as well as estimates for the surface coating thickness, yields dimensions in good agreement with DLS data indicating the IONCs are well dispersed and nonaggregated (Figure 2b, Tables 1 and S1). After transfer into water, or other physiologically relevant media, there are no visible precipitates over days.

3.2. Colloidal Stability of Iron Oxide Nanocrystals. The average core size and morphology of the iron oxide nanocrystals (IONCs) coated and in aqueous solutions are identical to those observed for as synthesized IONCs (Figures 1a-d and S1). Moreover, dynamic light scattering (DLS) and TEM image analysis reveal that water-soluble IONCs are well dispersed. They do not cluster or aggregate, and their dimensions increase as the surface coating thickness increases (Figures 2b and S1, Tables 1 and S1). As nanocrystal core size increases from 4 to 33 nm, the hydrodynamic diameter of phase transferred IONCs coated with oleic acid bilayer increases from 16 to 41 nm with a uniform average coating thickness of approximately 5.2 ± 0.7 nm (Figure 2b and Table 1)—the approximate length of two oleic acid molecules (~4.8 nm). With larger molecular weight polymer surface coatings, the IONCs have much larger HD sizes (~19-69 nm) with less uniform coating thicknesses from approximately 7.5 to 22 nm (Figure 2b and Table 1). The average zeta potentials for oleic acid bilayer, PAA-LA, PAMPS-LA, and PMAO-PEG coated IONCs are -48.3 ± 8.7 , -55.8 ± 8.6 , -51.7 ± 8.5 , and -45.0 \pm 7.0 mV, respectively.

Encapsulated IONCs, coated with oleic acid, PAA-OA, PMAO-PEG, and PAMPS-LA, are colloidally stable in a range of physiologically relevant media like deionized water (DI water), phosphate buffer saline (PBS), Dulbecco's modified Eagle medium (DMEM), Roswell Park Memorial Institute medium (RPMI), and borate buffer (B.B) (Figure 2c). Similarly, these materials maintain their colloidal stability under a wide range of pH conditions (5–10) and at high monovalent salt concentrations (0.05–0.5 M NaCl) (Figure 2d,e). When polymer surface coatings contained carboxylate functionality, however, the materials lost colloidal stability under highly acidic conditions (pH 3) and in the presence of high divalent salt concentrations (0.05–0.5 M CaCl₂) (Figure 2d,f). The relatively high pK_a of most organic acids suggests these functional groups may protonate at lower pH, removing

any electrostatic stabilization of the IONCs; additionally, divalent metal cations like Ca2+ can interact with these groups and bridge between nanocrystals causing aggregation. 69,70 PMAO-PEG encapsulated nanocrystals behave similarly as anhydride functional groups are hydrolyzed to carboxyl groups especially at low pH and in the presence divalent metal cations. Phase transferred nanocrystals with sulfonate-containing polymer coatings (PAMPS-LA) provide for the most stable suspensions under all conditions—even low pH and high CaCl₂ (0.05-0.5 M) conditions. This is to be expected for sulfonated polymers because of their low pK_a (<2), hydrogen bond donor and acceptor properties, and lack of interaction with divalent cations. 69-74 As such, relatively novel sulfonated polymeric surface coatings like PAMPS-LA demonstrate significant promise in biomedical applications of nanomaterials.^{71-73,75}

3.3. T_2 Relaxation Dynamics of Iron Oxide Nanocrystals Depend on the Core Dimension and Surface Coating Structure. 3.3.1. Magnetic Nanocrystal T_2 Relaxation Theory. In the presence of an external magnetic field, iron oxide nanocrystals (IONCs) induce inhomogeneous local magnetic fields that shorten the T_2 of water protons. The concentration-dependent capacity of IONCs to accelerate the transverse relaxation rate $(1/T_2)$ of water protons is called T_2 relaxivity, or r_2 (mM $^{-1}$ s $^{-1}$), and is a widely accepted metric of IONC contrast agent performance. The interaction between magnetic nanocrystals and local water protons is dominated by outer sphere relaxation mechanisms, so r_2 can be approximated by an outer sphere model termed the motional averaging regime (MAR). This results in the following relationship:

$$r_2 = \frac{4\nu_{\text{mat}}(\gamma_{\text{H}}\mu_0 M_{\text{v}} d)^2}{405D_{\text{bulk}}}$$
(2)

where $\gamma_{\rm H}$ is the water ¹H nuclei gyromagnetic ratio (2.68 × 10⁸ rad T⁻¹ s⁻¹), μ_0 is the permeability of a vacuum ($4\pi \times 10^{-7}$ T m A⁻¹), D is the translational diffusion constant of water ($D_{\rm bulk} = 3.1 \times 10^{-9}$ m² s⁻¹ at 37 °C), $\nu_{\rm mat}$ is the molar volume of magnetic ions, d is the nanocrystal diameter (m), and $M_{\rm v}$ is the volumic saturation magnetization (A m⁻¹).^{22–24}Equation 2 is a valid approximation of r_2 only when a nanocrystal's localized magnetic field ($\Delta\omega = \gamma_{\rm H}\mu_0M_{\rm v}/3$), and the time it takes water to diffuse through the characteristic dimensions of that field ($\tau_{\rm D} = d^2/4D_{\rm bulk}$) is sufficiently small.^{3,22–25,76} This criterion is referred to as the Redfield condition ($\Delta\omega\tau_{\rm D} \ll 1$). This

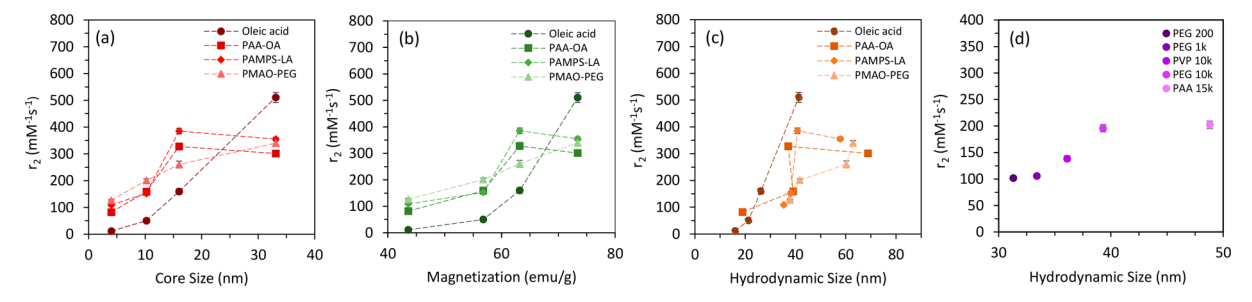


Figure 3. Plots of r_2 values of iron oxide nanocrystals. Plots of r_2 values of iron oxide nanocrystals depending on their core diameters (a) and hydrodynamic size (c). The r_2 values of 10 nm core iron oxide nanocrystals with different molecular weight of polymers and hydrodynamic size.

condition is easily met for smaller nanocrystal contrast agents. With increasing IONC dimension the strength and volume of the perturbed magnetic field increase and result in a substantial increase in the transverse proton relaxation rate $(1/T_2)$ of freely diffusing water. When the Redfield condition is met, increases in both the magnetic nanocrystal core size (d) and its volumic saturation magnetization $(M_{\rm v})$ are the only relevant material parameters for increasing contrast agent performance, or r_2 . ^{22–24,76} Nanocrystal clustering can also significantly impact r_2 by altering the effective particle size (d). ^{24,29,77} We note that iron oxide nanocrystals made through this route, and modified with these types of surfaces, have been reported to be highly uniform and nonaggregating. ^{60,65,68}

The dynamics described by eq 2 are no longer applicable once the time water spends near a magnetized core equals or exceeds the relaxation time ($\Delta\omega\tau_{\rm D}>1$). When these times are approximately equal, the static dephasing regime (SDR) can be easily identified in size-dependent studies of T₂ relaxivity as a peak or plateau. ^{23,24,29,78} In other words, SDR describes conditions in which freely diffusing water molecules experience the nanocrystal's field for the entire duration of the T₂ measurement (Scheme 1a). At even larger dimensions of contrast agent, ($\Delta\omega\tau_{\rm D}>20$), the time water spends dephasing within the field around IONCs becomes so long that it exceeds the interval between echoes in a T₂-weighted spin echo MRI sequence, reducing signal production. In this echo limited regime (ELR) r_2 decreases with increasing IONC dimension and is a condition best avoided in the design of contrast agents. ^{3,22,23,25,76}

Contrast agents that are just large enough to be described well by the static dephasing regime (SDR) have the largest relaxivity. For a magnetite (Fe₃O₄) contrast agent ($M_{v(bulk)}$ = 4.76×10^5 A m⁻¹), the SDR model would predict a theoretical maximum r_2 of approximately 960 mM⁻¹ s⁻¹.^{76,79} As the perweight saturation magnetization of a nanocrystal is reduced by at least 10% from the bulk value due to surface disorder, a more reasonable estimate for optimum IONC contrast agents performance would be an r_2 of 860 mM⁻¹ s⁻¹.⁸⁰ The smallest core diameters for which the SDR plateau is reached (Scheme 1a) can be estimated from the Redfield condition. Assuming a fixed $\Delta\omega\tau_{\rm D}$ = 5–20 and a magnetite IONC with 10% less saturation magnetization than bulk magnetite, this dimension, defined here as d_{SDR} , is between 36 and 72 nm. This is in reasonable agreement with experimental studies showing nonaggregated iron oxide nanocrystals reach SDR at core diameters of roughly 50 nm.^{24,78}

Several recent efforts have extended the models described above to include the impact of nonmagnetic surfaces on water proton spin dynamics. Impermeable surface coatings, such as dense silica and natural latex rubber, limit access of water to the nanocrystal's inhomogeneous field and therefore decrease r_2 with increasing thickness. So,51 Bao et al. modified eq 2 to account for this "exclusion radius" and explicitly introduced a coating thickness into the calculation of r_2 . However, many IONC surface coatings are hydrophilic polymers that would interact with, rather than exclude, bulk water. Bao et al. recognized that these coatings would offer "slow compartments" for water diffusion whose impact would depend on the hydrophilicity, thickness, as well as density of the permeable coating. We explicitly modify eq 2 to account for an effective water diffusion constant as a way to capture the overall impact on relaxivity:

$$r_2 = C \frac{(M_{\rm v}d)^2}{D_{\rm effective}} \tag{3}$$

where $D_{\rm effective}$ is the average reduced diffusion constant reflecting the time bulk water slows down as it interacts with the coating, and C is a coefficient that captures relevant constants in eq 2 for magnetite ($C=0.0166~{\rm m}^{\rm S}~{\rm mol}^{-1}~{\rm s}^{-2}~{\rm A}^{-2}$). This modified MAR model suggests another approach to the optimization of the relaxivity of a T_2 contrast agent. If water slows down and spends more time in the inhomogeneous magnetic field around the particle, then the contrast agent relaxivity can be increased—something Gossuin et al. successfully demonstrated using different solvents and solution temperatures. ⁸³

An important consequence of introducing a slower diffusion time for water is that the transition from the MAR to the SDR regime will occur at a smaller core dimension. With effective diffusion constants smaller than bulk water, then the time spent around the particle increases accordingly as $\tau_{\rm D}=d^2/4D_{\rm effective}$ where d is nanocrystal core diameter. Slowing water down with a strong surface coating interaction makes it possible to achieve the static dephasing regime (5 < $\Delta\omega\tau_{\rm D}$ < 20) at slightly smaller core diameters (Scheme 1b). For example, assuming the diffusion constant of water is reduced by 10% because of a water-permeable surface coating, then the critical IONC diameter to reach the static dephasing plateau goes from 36 to about 34 nm.

3.3.2. Surface-Coating Dependence of Nanocrystal T_2 Relaxation Dynamics. The libraries of surface coated IONCs synthesized (sections 3.1 and 3.2) allow us to test the impact of water permeable coatings over the different spin dynamics regimes relevant for creating T_2 contrast. We first confirmed the diameter dependent trends expected for the motional averaging regime (MAR) are observed over a range of iron oxide nanocrystal dimensions (Figure S2). The relaxivity (r_2) of different diameter IONCs (4–33 nm) with four types of surface coatings (oleic acid, PAA-OA, PAMPS-

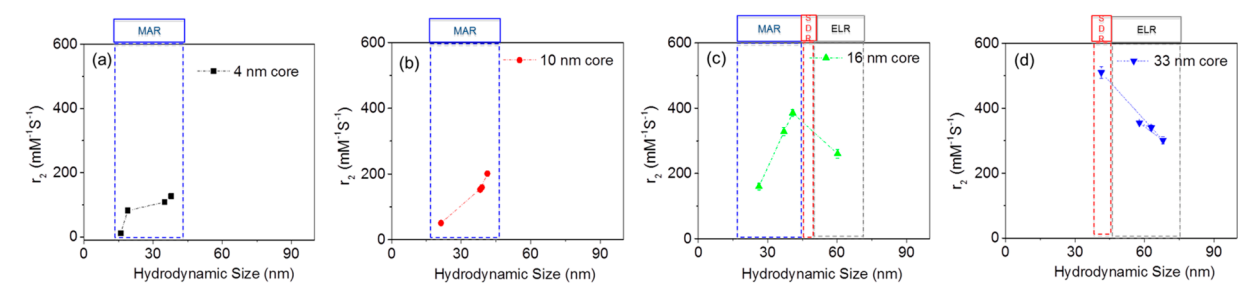


Figure 4. Relaxivity of iron oxide nanocrystals with different cores (4, 10, 16, and 33 nm) (a–d). The points indicate the surface coatings oleic acid bilayer, PAA-OA, PAMPS-LA, and PMAO-PEG, respectively (left to right). The samples have an increase in hydrodynamic diameter, as measured by dynamic light scattering, because the different polymer coatings vary in their molecular weight. Above the graphs the relevant dynamical regime is noted; MAR (motional averaging regime), SDR (static dephasing regime), ELR (echo limited regime).

Table 2. Summary of Relevant Physiochemical, Magnetic, and Relaxometric Parameters for IONCs Reported Here and the Highest Performing, Single Core, Spherical Iron Oxide Nanocrystal T₂ MRI Contrast Agents Found in the Literature

Reference	Surface Coating	Core Size (nm)	HD (nm)	$\frac{M_{\rm v}(10^5{\rm A}}{{ m m}^{-1})^n}$	$r_2(\mathrm{mM}^{-1}\mathrm{s}^{-1})$	$\Delta\omega au_{ m D}$	$d_{\rm SDR}({ m nm})^o$
Lee et al.	DMSA	12	-	3.79 ^h	218 ^{a,h}	0.681	46.0
Jang et al.	DMSA	15	~17.5	4.27 ^b	$276^{a,k}$	1.14^{m}	44.5
Vuong et al.	PAA (5k)	17.8	-	3.27^{f}	292.6 ^{c,d}	0.97	50.8
Mohapatra et al.	BPEI	16	48	$4.30^{b,j}$	297 ⁱ	1.30 ^m	49.9
Lartigue et al.	Rhamnose	18.5	23.6	3.37 ^b	$\sim 300^{a,h}$	1.31 ^m	50.1
Nandwana et al.	NDOPA-PEG	8.1	34	2.64 ^{b,e}	355 ⁱ	0.20^{m}	56.6
LaConte et al.	DSPE-PEG750	13.6	10.35	-	$360^{a,d}$	-	-
Tong et al.	DSPE-mPEGIOOO	14	28.6	-	$385^{c,d}$	-	-
This work	Oleic acid, PAA-OA, PAMPS-LA,PMAO-PEG	4.0	16.0-37.8	$2.26^{b,f}$	11.1-126.6 ^{<i>p</i>,<i>g</i>}	0.04^{m}	61.3
		10.2	21.3-41.7	2.94 ^{b,f}	50.5-201.1 ^{<i>p</i>,<i>g</i>}	0.36^{m}	53.7
		16.0	26.2-60.2	$3.27^{b,f}$	159.8-385.2 ^{p,g}	0.99^{m}	50.9
		33.1	41.3-68.8	3.80 ^{b,f}	301.2-510.3 ^{p,g}	4.92 ^m	47.2

"Room temperature (15–25 C). ^b27 C. ^c40 C. ^d0.47 T. ^e0.5 T. ^f1 T. ^g1.41 T. ^h1.5 T. ⁱ3 T. ^j4 T. ^k4.7 T, ^lD25C = 2.25 × 10⁻⁹ m² s⁻¹, ^mD27C = 2.37 × 10⁻⁹ m² s⁻¹, ⁿ $\rho_{\text{magnetite}}$ = 5.18 × 106 g m⁻³ assumed for conversions from M_{s} (emu g⁻¹) to M_{v} (A m⁻¹), ^o $\Delta\omega\tau_{\text{D}}$ = 10 assumed for d_{SDR} calculations, and ^p37 C. 2,3-dimercaptosuccinic acid (DMSA), polyvinylpyrrolidone (PVP), branched polyethyleneimine (BPEI), poly(acrylic acid) (PAA), glycol (PEG), methoxy-PEG (mPEG), nitrodopamine (NDOPA), l,2-distearoyl-sn-glycero-3-phosphoethanolamine (DSPE), octylamine (OA), poly(2-acrylamido-2-methylpropane sulfonic acid) (PAMPS), lauryl acrylate (LA), poly(maleic anhydride-alt-1-octadecene) (PMAO), T_2 relaxivity (r_2), mass saturation magnetization (M_{s}), and volumic saturation magnetization (M_{v}).

LA, and PMAO-PEG) was found from the slope of iron concentration versus $1/T_2$ plots measured at 1.41 T (Figure S3, Table 1). Consistent with the motional averaging regime we find that for all surface coatings, r_2 increases with core diameter (d), volumic saturation magnetization (M_v) , and hydrodynamic size at smaller sizes (Figures 3a-c and S4).^{24,84} This trend is most evident for the oleic acid bilayer coated nanocrystals whose r_2 values increase from 11 to 510 mM⁻¹ s⁻¹ as their core size increases from 4 to 33 nm (Table 1). The exceptional performance of the 33 nm oleic acid IONCs results from their large core size and thin, bilayer coating (5.2 \pm 0.7 nm), approximating well our calculation of $d_{\rm SDR}$ for a bare magnetite nanocrystal (36 nm). This thin coating leads to a very small "slow compartment" for water diffusion and $\tau_{\rm D}$ is therefore minimized, allowing r_2 to continue increasing with core diameter consistent with MAR.

Polyacrylate (PAA-OA) and polysulfonate (PAMPS-LA) coated IONCs of smaller dimensions also show an increase in relaxivity, r_2 , with core dimension, indicative of a motional averaging regime; however, the largest 33 nm diameter IONC for these surface coatings is in the static dephasing regime, SDR (Figure 3a,c). The experimental data brackets the $d_{\rm SDR}$ between 16 and 33 nm diameter for these systems. These thick water-permeable polymeric coatings will interact with water, increasing the time water spends in the nanocrystal's localized

field (τ_D) , thus shifting $d_{\rm SDR}$ to smaller core sizes. As a result, the peak r_2 for PAA-OA and PAMPS-LA coated IONCs (327.7 and 385.2 mM⁻¹ s⁻¹, respectively) occurs at a smaller core dimension (16–33 nm) than observed for the thinner oleic bilayer coatings (33 nm) (Table 1).

Additional evidence for the importance of water interactions with the IONC surface coatings can be found from the impact of surface thickness on contrast performance. Figure 4 shows the relaxivity for the different core dimensions as a function of the hydrodynamic diameter of the different coatings, with oleic acid being the thinnest at 5.2 ± 0.7 nm and PMAO-PEG being the thickest at 17.5 ± 2.8 nm. For smaller core sizes (4 and 10 nm), the motional averaging regime dominates as water is not spending a significant amount of time diffusing through the nanocrystal's localized field (MAR; $\Delta\omega\tau_{\rm D}\ll 1$); in this limit, increasing coating thickness will increase the dimensions of the slow compartment, thereby increasing r_2 . Similar behavior is seen for 10 nm IONCs coated with coating of increasing molecular weight (PEG 200-10k, and PVP 10k) (Figure 3d, Table S1). For larger core diameters (16 nm) the static dephasing regime can dominate, and coating thickness no longer plays a role in optimizing relaxivity. For the largest core diameters (33 nm), water is already spending its entire relaxation time in the nanocrystal's field (SDR; 5 < $\Delta\omega\tau_{\rm D}$ < 20), and thicker coatings will push the system into the

unfavorable echo limited regime (ELR). These data illustrate that if the core diameters are small enough that the IONC is well described by MAR then increasing a permeable coating thickness can be an effective strategy for increasing contrast agent performance (Figure 4a-c). For larger core diameters, however, already in SDR such surface coating changes can reduce the relaxivity of contrast agents (Figure 4c,d).

Coating density can also play a role in defining water's interaction with IONCs as illustrated by comparing the diameter-dependent relaxivity of IONC cores covered with a very low-density coating, PMAO-PEG, to the higher density PAA-OA and PAMPS-LA. Density here refers to grafting density which is the number of polymer chains bound to a nanocrystal. For linear polymer coatings grafted to particles, an increase in molecular weight will lead to a decrease in the number of chains bound to a nanocrystal surface. 60,64 The molecular weight of oleic acid, PAA-OA, PAMPS-LA, and PMAO-PEG phase transfer agents are 283, 2783, 4615, and 30,000-50,000 Da, respectively (Figure S5, Table S2) and because of its large molecular weight PMAO-PEG has very few polymer chains (~12 molecules/IONC) bound to the nanocrystals (Figure S6 and Table S2). IONC cores treated with this sparse coating do not reach the static dephasing regime even at the largest core diameters (Figure 3c). We speculate that with such little polymer coating present, there is less interaction with water and as a result water diffusion is not impacted in the near-particle region. A consideration of the grafting density of surface coatings could help rationalize similarly complex surface-dependent trends in r₂ found elsewhere.53-

Table 2 summarizes the performance (r_2) of the IONC contrast agents examined here compared to previously published reports of single core, spherical IONC of similar structure. 27,28,30-38,57-59 As a group, these IONCs have T₂ relaxivities much greater than commercial agents (<200 mM⁻¹ s⁻¹). In addition, the samples studied here compare well to those reported by others and one, the largest oleic acid bilayer coated sample, has to our knowledge the largest reported r_2 $(510.3 \text{ mM}^{-1} \text{ s}^{-1})$ for spherical iron oxide monocrystals (Table 2). 27,28,30–38,57–59 Accounting for both core size and saturation magnetization by using the Redfield parameter ($\Delta \omega \tau_{\rm D}$), we can estimate the relevant relaxation regimes for these materials. All these high-performing materials fall just short of the static dephasing regime ($\Delta\omega\tau_{\rm D}\approx 1$). If effective diffusion constants (D_{eff}) are used instead of bulk diffusion constants (D_{bulk}) , and we assume perhaps a 20% reduction in water diffusion due to surface coating effects, the Redfield parameter ($\Delta \omega \tau_{\rm D}$) would be larger and more accurately place these materials closer to SDR. This could help explain why the NDOPA-PEG IONCs reported by Nandwana et al. have one of the largest relaxivities despite having the lowest Redfield parameter $(\Delta \omega \tau_D)$. For our surface-coated IONCs most obviously in MAR, $D_{\rm eff}$ is approximately 20% lower than D_{bulk} which increases τ_{D} and $\Delta\omega\tau_{\rm D}$ by roughly 25% (Figure 5). Given our surface-coated IONCs are well-dispersed, the effects of clustering on $\tau_{\rm D}$ are not likely significant here (Figure 2b and S1, Tables 1 and S1). Depending on the physiochemical parameters of the surface coating, the deceleration of water diffusion in the coating could be even more significant. 52,81,82 This analysis also helps explain why every IONC in Table 2 exhibits the optimal r2 at a core size much smaller than their predicted $d_{\rm SDR}$ (for $\Delta \omega \tau_{\rm D}$ = 10) – the diffusion of water through hydrophilic surface coatings allows for longer interactions with the inhomogeneous

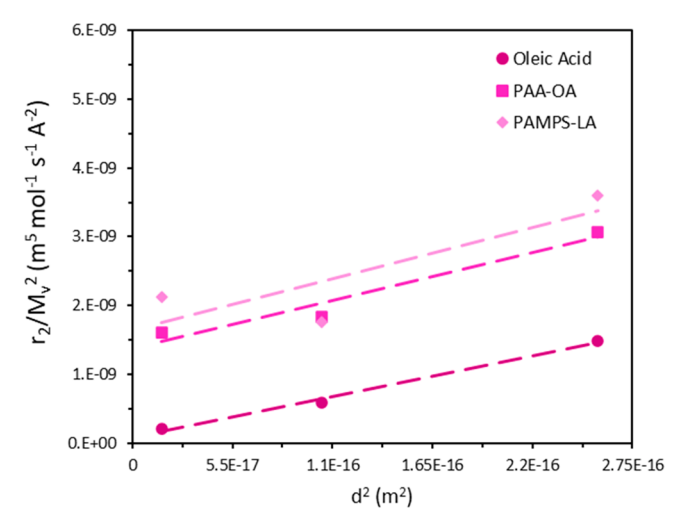


Figure 5. Using eq 3, $C/D_{\rm effective}$ and therefore $D_{\rm effective}$ can be approximated from the slope of the line generated from a plot of $r_2/M_{\rm v}^2$ as a function of d^2 for each coating using samples in MAR (according to Figure 4). The $D_{\rm effective}$ for the oleic acid bilayer (R^2 = 0.9959) and the polymer PAA-OA (R^2 = 0.9589) are linear enough to allow for an estimation of the diffusion constant in the polymer coatings. These are roughly $(3.1 \pm 0.45) \times 10^{-9}$ and $(2.6 \pm 0.26) \times 10^{-9}$. Since the oleic acid bilayer coating is thin and likely impermeable to water, its $D_{\rm effective}$ can be used as an approximation of $D_{\rm bulk}$ for the conditions of our nanocrystal solutions. Therefore, the $D_{\rm effective}$ for larger polymer coatings like PAA-OA is approximately 79–85% of $D_{\rm bulk}$.

magnetic field near the IONCs. This analysis suggests that if core diameter and material saturation magnetization are held constant, and the material is small enough to be in the motional averaging regime, then contrast performance can be optimized with surface coating thickness and/or grafting density.

3.3.3. Dependence of Iron Oxide Nanocrystal T₂ Relaxation Dynamics on the Solution Chemistry. While the relaxivity characterization presented thus far was completed in pure water (Table 1, Figure 3, and Figure 4), the solution environment for IONCs can be very different in vivo. The presence of salts and proteins can lead to aggregation of IONCs, for example (Figure 2c-f), with consequences for their contrast agent performance. We find that the iron oxide nanocrystal (IONCs) T2 relaxivity changes in different media tracks well with their colloidal stability (Figure 2c-f and Figure 6a-d). Uncontrolled IONC aggregation drastically increases physical dimensions leading to a decrease in r_2 as the T_2 dynamics, with properties better described by the ELR regime. Across various buffer solutions and under a range of pH (5-10) and monovalent salt concentrations (0.05-0.5 M NaCl), colloidally stable IONCs mostly maintain their high T2 relaxivity $(r_2 \ge \sim 200 \text{ mM}^{-1} \text{ s}^{-1})$ (Figure 2c-e and Figure 6a-c). Notably, IONCs with carboxylate-containing encapsulation agents (oleic acid bilayer, PAA-LA, and PMAO-PEG) have a significantly reduced r₂ under highly acidic conditions (pH 3) and in the presence of high divalent salt concentrations (0.05-0.5 M CaCl₂) (Figure 2d,f and Figure 6b,d). As discussed above, carboxylate-containing surface coating agents become less stable at low pH and in the presence of divalent metal cations like Ca²⁺, leading to aggregation and a reduction in r_2 . ^{69,70} The sulfonated polymer coatings in contrast maintain good colloidal stability and high T2 performance under all

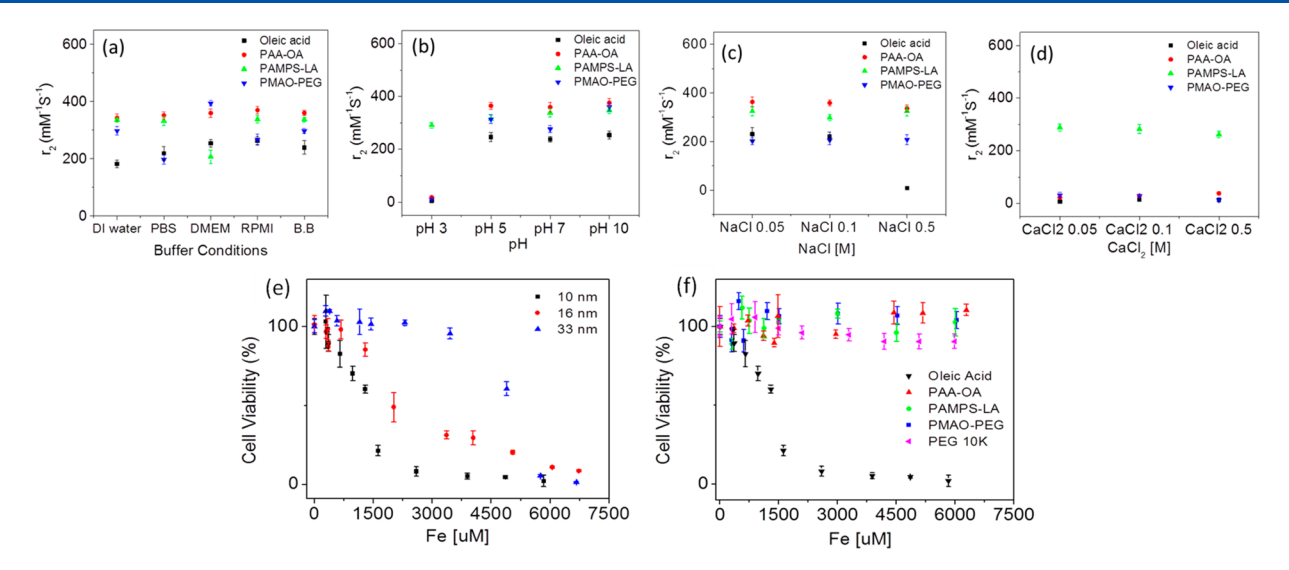


Figure 6. r_2 of iron oxide nanocrystals (10 nm) dispersed in different (a) buffer solutions (distilled ionized water (DI water), phosphate buffer saline (PBS), Dulbecco's modified Eagle's medium (DMEM) and Roswell Park Memorial Institute medium (RPMI), and borate buffer (B.B)), (b) pH 3–10, (c) NaCl 0.05–0.5 M, and (d) CaCl₂ 0.05–0.5 M. *In vitro* cell viability assays (MTS) of oleic acid coated iron oxide nanocrystals with (e) different core sizes (10, 16, 33 nm) and (f) 10 nm iron oxide nanocrystals with various surface coatings (oleic acid bilayer, PAA-OA, PAMPS-LA, PMAO–PEG, and 10k PEG).

conditions—even at low pH and high $CaCl_2$ (0.05–0.5 M). $^{69-74}$

3.4. Size- and Surface Coating-Dependent Cytotoxicity of Iron Oxide Nanocrystals. Iron oxide particles are FDA-approved as MRI contrast agents reflecting their good biocompatibility.⁸⁵ While these materials are similar to those commercially used, there is always a concern that new formulations of relatively benign nanomaterials could present some toxicity. If novel surface coatings promoted particle dissolution, then released free iron could disrupt iron homeostasis; alternatively, under some circumstances nanocrystals can promote proinflammatory responses leading to oxidative stress and acute cytotoxicity. 6,86-91 We conducted a preliminary in vitro experiment to identify any core diameter or surface coating cytotoxicity trends using our expansive library of IONCs. A simple and standard assay was used to assess the viability of human dermal fibroblast cells after 24 h in the presence of increasing concentrations IONCs with varied dimensions (10-33 nm) and surface coatings (oleic acid bilayer, PAA-OA, PAMPS-LA, PMAO-PEG, and 10k PEG) (Figure 6e,f).

Except for the oleic acid bilayer coated IONCs, there was no significant cytotoxic effects up to concentrations of 6.00 mM (335 ppm atomic Fe). This null cytotoxicity result necessarily limits our analysis of diameter and surface coating trends for most of these materials. The one exception is the bilayercoated IONCs which at very highest concentrations did have a significant effect on cell viability. We speculate that this amphiphilic coating is more prone to biological transformations and may also have increased interactions with cell membranes.^{6,86-91} For IONC coated with these bilayers the material cytotoxicity increased with decreasing core dimension, a trend observed in many in vitro cytotoxicity studies of metal oxide nanocrystals (Figure 6e). 92 The greater toxicity of smaller particles has been attributed to factors related to cellular uptake as well as more pronounced dissolution of smaller cores.^{6,86–91}

4. CONCLUSIONS

This study probes the size and surface coating-dependent relaxation dynamics of iron oxide nanocrystals (IONCs) to optimize their performance as T2 MRI contrast agents. Synthesized IONCs are monodispersed, size tunable (4-33 nm), and are easily transferred into aqueous solution using a variety of hydrophilic surface coating agents (oleic acid bilayer, PAA-OA, PAMPS-LA, PMAO-PEG, PEG 200-10 k, PVP 10k, and PAA 15k). Phase transferred nanocrystals display good colloidal stability under a range of physiologically relevant conditions. Relaxation dynamics data indicate that maximal r_2 can be achieved by tuning surface coating-dependent water diffusion constants ($D_{\text{effective}}$) with coating thickness and grafting density. Future work will use NMR dispersion (NMRD) experiments and relaxation simulations to further elaborate and quantify the observed effects. IONCs with a large core size (33 nm) and thin surface coating (oleic acid bilayer) have the highest reported T₂ relaxivity for this class of materials ($r_2 = 510 \text{ mM}^{-1} \text{ s}^{-1}$). Their r_2 values are stable under a variety of solution conditions and demonstrate no significant cytotoxicity in human dermal fibroblasts at iron concentrations as high as 1200 µM. Thicker, lower grafting density surface coatings (PAA-OA, PAMPS-LA, and PMAO-PEG) exhibit no significant cytotoxicity at iron concentrations as high as 6,000 μ M and retain high and stable r_2 (>300 mM⁻¹ s⁻¹) over a range of similar solution conditions. Poly sulfonated coatings, PAMPS-LA, yielded IONCs with good colloidal stability and high r₂ even under the harshest conditions tested (pH 3 and $0.05-0.1 \text{ M CaCl}_2$).

These data offer some insight into the rational design of T_2 contrast agents for advanced MRI applications. For molecular imaging, the ideal nanocrystal hydrodynamic diameter is between 5 and 50 nm to allow for optimal blood circulation times. ⁹³ Fortunately this size range coincides roughly with the static dephasing regime for these IONCs, leading to an optimized T_2 performance. Commercial IONCs used as MRI contrast agents are generally within this size range but exhibit much lower r_2 values (<200 mM⁻¹ s⁻¹)—likely because of

smaller core sizes, poor sample uniformity, and unoptimized surface coatings. 4,24 For the highest performance IONCs, the largest core size and smallest coating thickness possible—while still maintaining the static dephasing regime (SDR), colloidal stability, and low toxicity—are ideal. However, if a larger hydrodynamic diameter is needed for other reasons, then the coating grafting density can help to maintain a high r_2 . Finally, "smart" T₂ contrast agents could result if stimuli-responsive changes in surface coating—an intraparticle effect—rather than clustering-an interparticle effect-could be engineered to take IONCs into SDR. 5-19 IONCs could be designed to "turn on" (ELR to SDR; increasing r_2) or "turn off" (SDR to MAR; decreasing r_2) by reducing their coating thickness or grafting density (i.e., via degradation or shedding) in response to relevant biological conditions. Though not the focus of the present study, the design and application of this type of "smart" T_2 contrast agent will be explored in future studies.

ASSOCIATED CONTENT

Supporting Information

The Supporting Information is available free of charge at https://pubs.acs.org/doi/10.1021/acs.jpcc.2c05390.

TEM images of iron oxide nanocrystals (IONCs) phase transferred with different surface coating agents. Magnetization curves for IONCs with different core sizes. T_2 weighted 3 T MR phantom images of IONCs. T_2 relaxivities for IONCs coated with different molecular weight polymers. Molecular weight and grafting density data for different surface coatings (PDF)

AUTHOR INFORMATION

Corresponding Author

Vicki L. Colvin — Department of Chemistry, Rice University, Houston, Texas 77005, United States; Department of Chemistry and School of Engineering, Brown University, Providence, Rhode Island 02912, United States; orcid.org/0000-0002-8526-515X; Email: vicki_colvin@brown.edu

Authors

Minjung Cho – Department of Chemistry, Rice University, Houston, Texas 77005, United States; Department of Translational Imaging & Department of Nanomedicine, Houston Methodist Research Institute, Houston, Texas 77030, United States

Jake Villanova — Department of Chemistry and School of Engineering, Brown University, Providence, Rhode Island 02912, United States; Oorcid.org/0000-0003-3116-8204

Dylan M. Ines — Department of Chemistry and School of Engineering, Brown University, Providence, Rhode Island 02912, United States; orcid.org/0000-0003-0514-097X

Jingge Chen – Department of Chemistry and School of Engineering, Brown University, Providence, Rhode Island 02912, United States

Seung Soo Lee – Department of Chemistry, Rice University, Houston, Texas 77005, United States

Zhen Xiao — Department of Chemistry and School of Engineering, Brown University, Providence, Rhode Island 02912, United States; oorcid.org/0000-0002-3740-3546

Xiaoting Guo – Department of Chemistry and School of Engineering, Brown University, Providence, Rhode Island 02912, United States Joshua A. Dunn – Department of Chemistry and School of Engineering, Brown University, Providence, Rhode Island 02912, United States; orcid.org/0000-0003-2436-926X

Deanna D. Stueber – Department of Chemistry and School of Engineering, Brown University, Providence, Rhode Island 02912, United States

Paolo Decuzzi — Department of Translational Imaging & Department of Nanomedicine, Houston Methodist Research Institute, Houston, Texas 77030, United States; Laboratory of Nanotechnology for Precision Medicine, Fondazione Instituto Italiano di Tecnologia, Genoa 16163, Italy; orcid.org/0000-0001-6050-4188

Complete contact information is available at: https://pubs.acs.org/10.1021/acs.jpcc.2c05390

Author Contributions

M.C. and J.V. contributed equally to this work. S.S.L., J.C., and D.M.I. contributed equally to this work.

Notes

The authors declare no competing financial interest.

ACKNOWLEDGMENTS

This work was supported by the Advanced Energy Consortium (UTA/AEC BEG08-011), Environmental Protection Agency (SV-84001801-0), the National Institute of Health (R01EY030569), and the National Science Foundation (CMMI-1057906). Work by P.D. done while at Houston Methodist Research Institute but is now at Fondazione Instituto Italiano di Tecnologia.

REFERENCES

- (1) Wahsner, J.; Gale, E. M.; Rodriguez-Rodriguez, A.; Caravan, P. Chemistry of MRI Contrast Agents: Current Challenges and New Frontiers. *Chem. Rev.* **2019**, *119*, 957–1057.
- (2) Ni, D. L.; Bu, W. B.; Ehlerding, E. B.; Cai, W. B.; Shi, J. L. Engineering of Inorganic Nanoparticles as Magnetic Resonance Imaging Contrast Agents. *Chem. Soc. Rev.* **2017**, *46*, 7438–7468.
- (3) Zhou, Z. J.; Yang, L. J.; Gao, J. H.; Chen, X. Y. Structure-Relaxivity Relationships of Magnetic Nanoparticles for Magnetic Resonance Imaging. *Adv. Mater.* **2019**, *31*, 32.
- (4) Stueber, D. D.; Villanova, J.; Aponte, I.; Xiao, Z.; Colvin, V. L. Magnetic Nanoparticles in Biology and Medicine: Past, Present, and Future Trends. *Pharmaceutics* **2021**, *13*, 943.
- (5) Arami, H.; Khandhar, A.; Liggitt, D.; Krishnan, K. M. In Vivo Delivery, Pharmacokinetics, Biodistribution and Toxicity of Iron Oxide Nanoparticles. *Chem. Soc. Rev.* **2015**, *44*, 8576–8607.
- (6) Malhotra, N.; Lee, J.-S.; Liman, R. A. D.; Ruallo, J. M. S.; Villaflores, O. B.; Ger, T.-R.; Hsiao, C.-D. Potential Toxicity of Iron Oxide Magnetic Nanoparticles: A Review. *Molecules* **2020**, *25*, 3159.
- (7) Yeap, S. P.; Lim, J.; Ooi, B. S.; Ahmad, A. L. Agglomeration, Colloidal Stability, and Magnetic Separation of Magnetic Nanoparticles: Collective Influences on Environmental Engineering Applications. *J. Nanopart. Res.* **2017**, *19*, 368.
- (8) Gao, G. H.; Im, G. H.; Kim, M. S.; Lee, J. W.; Yang, J.; Jeon, H.; Lee, J. H.; Lee, D. S. Magnetite-Nanoparticle-Encapsulated Ph-Responsive Polymeric Micelle as an Mri Probe for Detecting Acidic Pathologic Areas. *Small* **2010**, *6*, 1201–1204.
- (9) Gallo, J.; Kamaly, N.; Lavdas, I.; Stevens, E.; Nguyen, Q. D.; Wylezinska-Arridge, M.; Aboagye, E. O.; Long, N. J. Cxcr4-Targeted and Mmp-Responsive Iron Oxide Nanoparticles for Enhanced Magnetic Resonance Imaging. *Angew. Chem., Int. Ed. Engl.* **2014**, *53*, 9550–9554.
- (10) Hsieh, V.; Okada, S.; Wei, H.; Garcia-Alvarez, I.; Barandov, A.; Alvarado, S. R.; Ohlendorf, R.; Fan, J. X.; Ortega, A.; Jasanoff, A.

- Neurotransmitter-Responsive Nanosensors for T-2-Weighted Magnetic Resonance Imaging. J. Am. Chem. Soc. 2019, 141, 15751–15754.
- (11) Li, F.; Liang, Z.; Liu, J.; Sun, J.; Hu, X.; Zhao, M.; Liu, J.; Bai, R.; Kim, D.; Sun, X.; Hyeon, T.; Ling, D.; et al. Dynamically Reversible Iron Oxide Nanoparticle Assemblies for Targeted Amplification of T1-Weighted Magnetic Resonance Imaging of Tumors. Nano Lett. 2019, 19, 4213–4220.
- (12) Liu, W.; Yin, S. Y.; Hu, Y. C.; Deng, T.; Li, J. S. Microemulsion-Confined Biomineralization of Pegylated Ultrasmall Fe3o4 Nanocrystals for T2-T1 Switchable Mri of Tumors. *Anal. Chem.* **2021**, 93, 14223–14230.
- (13) Lu, J. X.; Sun, J. H.; Li, F. Y.; Wang, J.; Liu, J. N.; Kim, D.; Fan, C. H.; Hyeon, T.; Ling, D. S. Highly Sensitive Diagnosis of Small Hepatocellular Carcinoma Using Ph-Responsive Iron Oxide Nanocluster Assemblies. *J. Am. Chem. Soc.* **2018**, *140*, 10071–10074.
- (14) Osborne, E. A.; Jarrett, B. R.; Tu, C. Q.; Louie, A. Y. Modulation of T2 Relaxation Time by Light-Induced, Reversible Aggregation of Magnetic Nanoparticles. *J. Am. Chem. Soc.* **2010**, *132*, 5934–5935.
- (15) Perez, J. M.; Josephson, L.; O'Loughlin, T.; Högemann, D.; Weissleder, R. Magnetic Relaxation Switches Capable of Sensing Molecular Interactions. *Nat. Biotechnol.* **2002**, *20*, 816–820.
- (16) Wu, B.; Deng, K.; Lu, S.-T.; Zhang, C.-J.; Ao, Y.-W.; Wang, H.; Mei, H.; Wang, C.-X.; Xu, H.; Hu, B.; Huang, S.-W. Reduction-Active Fe3o4-Loaded Micelles with Aggregation- Enhanced Mri Contrast for Differential Diagnosis of Neroglioma. *Biomaterials* **2021**, *268*, 120531.
- (17) Yigit, M. V.; Mazumdar, D.; Kim, H. K.; Lee, J. H.; Odintsov, B.; Lu, Y. Smart "Turn-on" Magnetic Resonance Contrast Agents Based on Aptamer-Functionalized Superparamagnetic Iron Oxide Nanoparticles. *Chembiochem* **2007**, *8*, 1675–8.
- (18) Yigit, M. V.; Mazumdar, D.; Lu, Y. Mri Detection of Thrombin with Aptamer Functionalized Superparamagnetic Iron Oxide Nanoparticles. *Bioconjugate Chem.* **2008**, *19*, 412–417.
- (19) Yuan, Y.; Ding, Z.; Qian, J.; Zhang, J.; Xu, J.; Dong, X.; Han, T.; Ge, S.; Luo, Y.; Wang, Y.; Zhong, K.; Liang, G. Casp3/7-Instructed Intracellular Aggregation of Fe3o4 Nanoparticles Enhances T2Mr Imaging of Tumor Apoptosis. *Nano Lett.* **2016**, *16*, 2686–2691.
- (20) Danhier, F. To Exploit the Tumor Microenvironment: Since the Epr Effect Fails in the Clinic, What Is the Future of Nanomedicine? *J. Controlled Release* **2016**, 244, 108–121.
- (21) Hingorani, D. V.; Bernstein, A. S.; Pagel, M. D. A Review of Responsive Mri Contrast Agents: 2005–2014. Contrast Media & Molecular Imaging 2015, 10, 245–265.
- (22) Brooks, R. A.; Moiny, F.; Gillis, P. On T2-Shortening by Weakly Magnetized Particles: The Chemical Exchange Model†. *Magn. Reson. Med.* **2001**, *45*, 1014–1020.
- (23) Gillis, P.; Moiny, F.; Brooks, R. A. On T(2)-Shortening by Strongly Magnetized Spheres: A Partial Refocusing Model. *Magn Reson Med.* **2002**, *47*, 257–263.
- (24) Vuong, Q. L.; Berret, J.-F.; Fresnais, J.; Gossuin, Y.; Sandre, O. A Universal Scaling Law to Predict the Efficiency of Magnetic Nanoparticles as Mri T2-Contrast Agents. *Adv. Healthcare Mater.* **2012**, *1*, 502–512.
- (25) Xiao, Y.; Du, J. Superparamagnetic Nanoparticles for Biomedical Applications. J. Mater. Chem. B 2020, 8, 354–367.
- (26) Kim, B. H.; Lee, N.; Kim, H.; An, K.; Park, Y. I.; Choi, Y.; Shin, K.; Lee, Y.; Kwon, S. G.; Na, H. B.; Park, J.-G.; Ahn, T.-Y.; Kim, Y.-W.; Moon, W. K.; Choi, S. H.; Hyeon, T. Large-Scale Synthesis of Uniform and Extremely Small-Sized Iron Oxide Nanoparticles for High-Resolution T1Magnetic Resonance Imaging Contrast Agents. J. Am. Chem. Soc. 2011, 133, 12624–12631.
- (27) Jun, Y.-w.; Huh, Y.-M.; Choi, J.-s.; Lee, J.-H.; Song, H.-T.; Kim, S.; Yoon, S.; Kim, K.-S.; Shin, J.-S.; Suh, J.-S.; Cheon, J. Nanoscale Size Effect of Magnetic Nanocrystals and Their Utilization for Cancer Diagnosis Via Magnetic Resonance Imaging. *J. Am. Chem. Soc.* **2005**, 127, 5732–5733.
- (28) Lee, J.-H.; Huh, Y.-M.; Jun, Y.-w.; Seo, J.-w.; Jang, J.-t.; Song, H.-T.; Kim, S.; Cho, E.-J.; Yoon, H.-G.; Suh, J.-S.; Cheon, J. et al.

- Artificially Engineered Magnetic Nanoparticles for Ultra-Sensitive Molecular Imaging. *Nature Medicine* **2007**, *13*, 95–99.
- (29) Pöselt, E.; Kloust, H.; Tromsdorf, U.; Janschel, M.; Hahn, C.; Maßlo, C.; Weller, H. Relaxivity Optimization of a Pegylated Iron-Oxide-Based Negative Magnetic Resonance Contrast Agent for T2-Weighted Spin–Echo Imaging. ACS Nano 2012, 6, 1619–1624.
- (30) Choo, E. S. G.; Peng, E.; Rajendran, R.; Chandrasekharan, P.; Yang, C.-T.; Ding, J.; Chuang, K.-H.; Xue, J. Superparamagnetic Nanostructures for Off-Resonance Magnetic Resonance Spectroscopic Imaging. *Adv. Funct. Mater.* **2013**, *23*, 496–505.
- (31) de Moura, C. L.; Gallo, J.; Garcia-Hevia, L.; Pessoa, O. D. L.; Ricardo, N.; Banobre-Lopez, M. Magnetic Hybrid Wax Nanocomposites as Externally Controlled Theranostic Vehicles: High Mri Enhancement and Synergistic Magnetically Assisted Thermo/Chemo Therapy. *Chem.—Eur. J.* **2020**, *26*, 4531–4538.
- (32) He, J. P.; Liu, X. H.; Niu, D. C.; Chen, J. Z.; Qin, X.; Li, Y. S. Supramolecular-Based Pegylated Magnetic Hybrid Vesicles with Ultra-High Transverse Relaxivity. *Applied Materials Today* **2018**, *11*, 238–245.
- (33) Jang, J. T.; Nah, H.; Lee, J. H.; Moon, S. H.; Kim, M. G.; Cheon, J. Critical Enhancements of Mri Contrast and Hyperthermic Effects by Dopant-Controlled Magnetic Nanoparticles. *Angew. Chem., Int. Ed.* **2009**, *48*, 1234–1238.
- (34) Kostevsek, N.; Cheung, C. C. L.; Sersa, I.; Kreft, M. E.; Monaco, I.; Franchini, M. C.; Vidmar, J.; Al-Jamal, W. T. Magneto-Liposomes as Mri Contrast Agents: A Systematic Study of Different Liposomal Formulations. *Nanomaterials* **2020**, *10*, 889.
- (35) Lee, N.; Choi, Y.; Lee, Y.; Park, M.; Moon, W. K.; Choi, S. H.; Hyeon, T. Water-Dispersible Ferrimagnetic Iron Oxide Nanocubes with Extremely High R2 Relaxivity for Highly Sensitive in Vivo Mri of Tumors. *Nano Lett.* **2012**, *12*, 3127–3131.
- (36) Tromsdorf, U. I.; Bigall, N. C.; Kaul, M. G.; Bruns, O. T.; Nikolic, M. S.; Mollwitz, B.; Sperling, R. A.; Reimer, R.; Hohenberg, H.; Parak, W. J.; Forster, S.; Beisiegel, U.; Adam, G.; Weller, H. Size and Surface Effects on the Mri Relaxivity of Manganese Ferrite Nanoparticle Contrast Agents. *Nano Lett.* 2007, 7, 2422–2427.
- (37) Yang, L.; Ma, L.; Xin, J.; Li, A.; Sun, C.; Wei, R.; Ren, B. W.; Chen, Z.; Lin, H.; Gao, J. Composition Tunable Manganese Ferrite Nanoparticles for Optimized T2 Contrast Ability. *Chem. Mater.* **2017**, 29, 3038–3047.
- (38) Zhao, Z.; Zhou, Z.; Bao, J.; Wang, Z.; Hu, J.; Chi, X.; Ni, K.; Wang, R.; Chen, X.; Chen, Z.; Gao, J. Octapod Iron Oxide Nanoparticles as High-Performance T₂ Contrast Agents for Magnetic Resonance Imaging. *Nat. Commun.* **2013**, *4*, 2266.
- (39) Mohapatra, J.; Mitra, A.; Tyagi, H.; Bahadur, D.; Aslam, M. Iron Oxide Nanorods as High-Performance Magnetic Resonance Imaging Contrast Agents. *Nanoscale* **2015**, *7*, 9174–9184.
- (40) Xiao, Z.; Zhang, Q.; Guo, X.; Villanova, J.; Hu, Y.; Külaots, I.; Garcia-Rojas, D.; Guo, W.; Colvin, V. L. Libraries of Uniform Magnetic Multicore Nanoparticles with Tunable Dimensions for Biomedical and Photonic Applications. ACS Appl. Mater. Interfaces 2020, 12, 41932–41941.
- (41) Tromsdorf, U. I.; Bruns, O. T.; Salmen, S. C.; Beisiegel, U.; Weller, H. A Highly Effective, Nontoxic T1Mr Contrast Agent Based on Ultrasmall Pegylated Iron Oxide Nanoparticles. *Nano Lett.* **2009**, *9*, 4434–4440.
- (42) Cowger, T. A.; Tang, W.; Zhen, Z.; Hu, K.; Rink, D. E.; Todd, T. J.; Wang, G. D.; Zhang, W.; Chen, H.; Xie, J. Casein-Coated FeSc2 Nanoparticles with Superior R2 Relaxivity for Liver-Specific Magnetic Resonance Imaging. *Theranostics* **2015**, *S*, 1225–1232.
- (43) Ahmadpoor, F.; Masood, A.; Feliu, N.; Parak, W. J.; Shojaosadati, S. A.The Effect of Surface Coating of Iron Oxide Nanoparticles on Magnetic Resonance Imaging Relaxivity. *Frontiers in Nanotechnology***2021**, 3. DOI: 10.3389/fnano.2021.644734
- (44) Jedlovszky-Hajdú, A.; Tombácz, E.; Bányai, I.; Babos, M.; Palkó, A. Carboxylated Magnetic Nanoparticles as Mri Contrast Agents: Relaxation Measurements at Different Field Strengths. *J. Magn. Magn. Mater.* **2012**, *324*, 3173–3180.

- (45) Neto, D. M. A.; Freire, R. M.; Gallo, J.; Freire, T. M.; Queiroz, D. C.; Ricardo, N. M. P. S.; Vasconcelos, I. F.; Mele, G.; Carbone, L.; Mazzetto, S. E.; Banobre-Lopez, M.; Fechine, P. B. A. Rapid Sonochemical Approach Produces Functionalized Fe3o4 Nanoparticles with Excellent Magnetic, Colloidal, and Relaxivity Properties for Mri Application. *J. Phys. Chem. C* 2017, 121, 24206–24222.
- (46) Park, J. C.; Lee, G. T.; Kim, H.-K.; Sung, B.; Lee, Y.; Kim, M.; Chang, Y.; Seo, J. H. Surface Design of Eu-Doped Iron Oxide Nanoparticles for Tuning the Magnetic Relaxivity. *ACS Appl. Mater. Interfaces* **2018**, *10*, 25080–25089.
- (47) Liu, X. L.; Wang, Y. T.; Ng, C. T.; Wang, R.; Jing, G. Y.; Yi, J. B.; Yang, J.; Bay, B. H.; Yung, L.-Y. L.; Fan, D. D.; Ding, J.; Fan, H. M. Coating Engineering of Mnfe2o4 Nanoparticles with Superhigh T2 Relaxivity and Efficient Cellular Uptake for Highly Sensitive Magnetic Resonance Imaging. *Advanced Materials Interfaces* **2014**, *1*, 1300069.
- (48) Duan, H.; Kuang, M.; Wang, X.; Wang, Y. A.; Mao, H.; Nie, S. Reexamining the Effects of Particle Size and Surface Chemistry on the Magnetic Properties of Iron Oxide Nanocrystals: New Insights into Spin Disorder and Proton Relaxivity. *J. Phys. Chem. C* **2008**, *112*, 8127–8131.
- (49) Hu, F.; MacRenaris, K. W.; Waters, E. A.; Liang, T.; Schultz-Sikma, E. A.; Eckermann, A. L.; Meade, T. J. Ultrasmall, Water-Soluble Magnetite Nanoparticles with High Relaxivity for Magnetic Resonance Imaging. *J. Phys. Chem. C* **2009**, *113*, 20855–20860.
- (50) Joshi, H.; De, M.; Richter, F.; He, J.; Prasad, P.; Dravid, V. Effect of Silica Shell Thickness of Fe3o4 Siox Cor. Shell Nanostructures on Mri Contrast. *J. Nanopart. Res.* **2013**, *15*, 1−8.
- (51) Arsalani, S.; Guidelli, E. J.; Silveira, M. A.; Salmon, C. E. G.; Araujo, J. F. D. F.; Bruno, A. C.; Baffa, O. Magnetic Fe3o4 Nanoparticles Coated by Natural Rubber Latex as Mri Contrast Agent. J. Magn. Magn. Mater. 2019, 475, 458–464.
- (52) Paquet, C.; de Haan, H. W.; Leek, D. M.; Lin, H.-Y.; Xiang, B.; Tian, G.; Kell, A.; Simard, B. Clusters of Superparamagnetic Iron Oxide Nanoparticles Encapsulated in a Hydrogel: A Particle Architecture Generating a Synergistic Enhancement of the T2 Relaxation. ACS Nano 2011, 5, 3104–3112.
- (53) LaConte, L. E.; Nitin, N.; Zurkiya, O.; Caruntu, D.; O'Connor, C. J.; Hu, X.; Bao, G. Coating Thickness of Magnetic Iron Oxide Nanoparticles Affects R2 Relaxivity. *J. Magn Reson Imaging* **2007**, *26*, 1634–1641.
- (54) Nandwana, V.; Ryoo, S.-R.; Kanthala, S.; De, M.; Chou, S. S.; Prasad, P. V.; Dravid, V. P. Engineered Theranostic Magnetic Nanostructures: Role of Composition and Surface Coating on Magnetic Resonance Imaging Contrast and Thermal Activation. ACS Appl. Mater. Interfaces 2016, 8, 6953–6961.
- (55) Tong, S.; Hou, S.; Zheng, Z.; Zhou, J.; Bao, G. Coating Optimization of Superparamagnetic Iron Oxide Nanoparticles for High T2 Relaxivity. *Nano Lett.* **2010**, *10*, 4607–4613.
- (56) Zeng, J.; Jing, L.; Hou, Y.; Jiao, M.; Qiao, R.; Jia, Q.; Liu, C.; Fang, F.; Lei, H.; Gao, M. Anchoring Group Effects of Surface Ligands on Magnetic Properties of Fe3o4 Nanoparticles: Towards High Performance Mri Contrast Agents. *Adv. Mater.* **2014**, *26*, 2694–2698.
- (57) Mohapatra, J.; Zeng, F. H.; Elkins, K.; Xing, M. Y.; Ghimire, M.; Yoon, S.; Mishra, S. R.; Liu, J. P. Size-Dependent Magnetic and Inductive Heating Properties of Fe3o4 Nanoparticles: Scaling Laws across the Superparamagnetic Size. *Phys. Chem. Chem. Phys.* **2018**, 20, 12879—12887.
- (58) Norek, M.; Kampert, E.; Zeitler, U.; Peters, J. A. Tuning of the Size of Dy2o3 Nanoparticles for Optimal Performance as an Mri Contrast Agent. J. Am. Chem. Soc. 2008, 130, 5335–5340.
- (59) Pothayee, N.; Balasubramaniam, S.; Pothayee, N.; Jain, N.; Hu, N.; Lin, Y.; Davis, R. M.; Sriranganathan, N.; Koretsky, A. P.; Riffle, J. S. Magnetic Nanoclusters with Hydrophilic Spacing for Dual Drug Delivery and Sensitive Magnetic Resonance Imaging. *J. Mater. Chem. B* **2013**, *1*, 1142–1149.
- (60) Cho, M.; Sethi, R.; Ananta narayanan, J. S.; Lee, S. S.; Benoit, D. N.; Taheri, N.; Decuzzi, P.; Colvin, V. L. Gadolinium Oxide

- Nanoplates with High Longitudinal Relaxivity for Magnetic Resonance Imaging. *Nanoscale* **2014**, *6*, 13637–13645.
- (61) Yu, W. W.; Chang, E.; Falkner, J. C.; Zhang, J.; Al-Somali, A. M.; Sayes, C. M.; Johns, J.; Drezek, R.; Colvin, V. L. Forming Biocompatible and Nonaggregated Nanocrystals in Water Using Amphiphilic Polymers. J. Am. Chem. Soc. 2007, 129, 2871–2879.
- (62) Carr, H. Y.; Purcell, E. M. Effects of Diffusion on Free Precession in Nuclear Magnetic Resonance Experiments. *Phys. Rev.* **1954**, *94*, 630–638.
- (63) Meiboom, S.; Gill, D. Modified Spin-Echo Method for Measuring Nuclear Relaxation Times. *Rev. Sci. Instrum.* **1958**, 29, 688–691.
- (64) Benoit, D. N.; Zhu, H.; Lilierose, M. H.; Verm, R. A.; Ali, N.; Morrison, A. N.; Fortner, J. D.; Avendano, C.; Colvin, V. L. Measuring the Grafting Density of Nanoparticles in Solution by Analytical Ultracentrifugation and Total Organic Carbon Analysis. *Anal. Chem.* **2012**, *84*, 9238–9245.
- (65) Yu, W. W.; Falkner, J. C.; Yavuz, C. T.; Colvin, V. L. Synthesis of Monodisperse Iron Oxide Nanocrystals by Thermal Decomposition of Iron Carboxylate Salts. *Chem. Commun.* **2004**, 2306–2307.
- (66) Bosi, F.; Halenius, U.; Skogby, H. Crystal Chemistry of the Magnetite-Ulvospinel Series. *Am. Mineral.* **2009**, *94*, 181–189.
- (67) Lee, S. S.; Zhu, H.; Contreras, E. Q.; Prakash, A.; Puppala, H. L.; Colvin, V. L. High Temperature Decomposition of Cerium Precursors to Form Ceria Nanocrystal Libraries for Biological Applications. *Chem. Mater.* **2012**, *24*, 424–432.
- (68) Prakash, A.; Zhu, H.; Jones, C. J.; Benoit, D. N.; Ellsworth, A. Z.; Bryant, E. L.; Colvin, V. L. Bilayers as Phase Transfer Agents for Nanocrystals Prepared in Nonpolar Solvents. *ACS Nano* **2009**, *3*, 2139–2146.
- (69) Akaighe, N.; Depner, S. W.; Banerjee, S.; Sharma, V. K.; Sohn, M. The Effects of Monovalent and Divalent Cations on the Stability of Silver Nanoparticles Formed from Direct Reduction of Silver Ions by Suwannee River Humic Acid/Natural Organic Matter. *Science of The Total Environment* **2012**, 441, 277–289.
- (70) Ji, L.; Chen, W.; Zheng, S.; Xu, Z.; Zhu, D. Adsorption of Sulfonamide Antibiotics to Multiwalled Carbon Nanotubes. *Langmuir* **2009**, *25*, 11608–11613.
- (71) Cavus, S. Poly(Methacrylamide-Co-2-Acrylamido-2-Methyl-1-Propanesulfonic Acid) Hydrogels: Investigation of Ph- and Temperature-Dependent Swelling Characteristics and Their Characterization. *J. Polym. Sci., Part B: Polym. Phys.* **2010**, *48*, 2497–2508.
- (72) El-Mahdy, G. A.; Átta, A. M.; Al-Lohedan, H. A. Synthesis and Evaluation of Poly(Sodium 2-Acrylamido-2-Methylpropane Sulfonate-Co-Styrene)/Magnetite Nanoparticle Composites as Corrosion Inhibitors for Steel. *Molecules* **2014**, *19*, 1713–1731.
- (73) Gad, Y. H. Preparation and Characterization of Poly(2-Acrylamido-2-Methylpropane-Sulfonic Acid)/Chitosan Hydrogel Using Gamma Irradiation and Its Application in Wastewater Treatment. *Radiat. Phys. Chem.* **2008**, *77*, 1101–1107.
- (74) Zhang, X.; Zhang, Q.; Ma, T.; Liu, Q.; Wu, S.; Hua, K.; Zhang, C.; Chen, M.; Cui, Y.Enhanced Stability of Gold Magnetic Nanoparticles with Poly(4-Styrenesulfonic Acid-Co-Maleic Acid): Tailored Optical Properties for Protein Detection. *Nanoscale Res. Lett.* 2017, 12. DOI: 10.1186/s11671-017-2303-6
- (75) Stinnett, G.; Taheri, N.; Villanova, J.; Bohloul, A.; Guo, X.; Esposito, E. P.; Xiao, Z.; Stueber, D.; Avendano, C.; Decuzzi, P.; Pautler, R. G.; Colvin, V. L. 2d Gadolinium Oxide Nanoplates as T1Magnetic Resonance Imaging Contrast Agents. *Adv. Healthcare Mater.* **2021**, *10*, 2001780.
- (76) Lartigue, L.; Coupeau, M.; Lesault, M.Luminophore and Magnetic Multicore Nanoassemblies for Dual-Mode MRI and Fluorescence Imaging. *Nanomaterials (Basel)***2020**, *10*, 28
- (77) Roch, A.; Gossuin, Y.; Muller, R. N.; Gillis, P. Superparamagnetic Colloid Suspensions: Water Magnetic Relaxation and Clustering. *J. Magn. Magn. Mater.* **2005**, 293, 532–539.
- (78) Xie, X.; Zhang, C. Controllable Assembly of Hydrophobic Superparamagnetic Iron Oxide Nanoparticle with Mpeg-Pla Copoly-

mer and Its Effect on Mr Transverse Relaxation Rate. J. Nanomater. 2011, 2011, 152524.

- (79) Cullity, B. D.; Graham, C. D. Ferrimagnetism. Introduction to Magnetic Materials 2008, 175-195.
- (80) Demortière, A.; Panissod, P.; Pichon, B. P.; Pourroy, G.; Guillon, D.; Donnio, B.; Bégin-Colin, S. Size-Dependent Properties of Magnetic Iron Oxide Nanocrystals. Nanoscale 2011, 3, 225-232.
- (81) de Haan, H. W.; Paquet, C. Enhancement and Degradation of the R-2* Relaxation Rate Resulting from the Encapsulation of Magnetic Particles with Hydrophilic Coatings. Magn. Reson. Med. 2011, 66, 1759-1766.
- (82) Vergara, A.; Paduano, L.; Vitagliano, V.; Sartorio, R. Mutual Diffusion in Aqueous Solution of Poly(Ethyleneglycol) Samples. Some Comments on the Effect of Chain Length and Polydispersity. Phys. Chem. Chem. Phys. 1999, 1, 5377-5383.
- (83) Gossuin, Y.; Orlando, T.; Basini, M.; Henrard, D.; Lascialfari, A.; Mattea, C.; Stapf, S.; Vuong, Q. L. NMR Relaxation Induced by Iron Oxide Particles: Testing Theoretical Models. Nanotechnology 2016, 27, 155706.
- (84) Mues, B.; Buhl, E. M.; Schmitz-Rode, T.; Slabu, I. Towards Optimized MRI Contrast Agents for Implant Engineering: Clustering and Immobilization Effects of Magnetic Nanoparticles. J. Magn. Magn. Mater. 2019, 471, 432-438.
- (85) Bawa, R.Handbook of Clinical Nanomedicine; Pan Stanford Publishing, 2016.
- (86) Patil, U. S.; Adireddy, S.; Jaiswal, A.; Mandava, S.; Lee, B. R.; Chrisey, D. B. In Vitro/in Vivo Toxicity Evaluation and Quantification of Iron Oxide Nanoparticles. Int. J. Mol. Sci. 2015, 16, 24417-24450.
- (87) Kornberg, T. G.; Stueckle, T. A.; Coyle, J.; Derk, R.; Demokritou, P.; Rojanasakul, Y.; Rojanasakul, L. W. Iron Oxide Nanoparticle-Induced Neoplastic-Like Cell Transformation in Vitro Is Reduced with a Protective Amorphous Silica Coating. Chem. Res. Toxicol. 2019, 32, 2382-2397.
- (88) Avramescu, M. L.; Rasmussen, P. E.; Chénier, M.; Gardner, H. D. Influence of Ph, Particle Size and Crystal Form on Dissolution Behaviour of Engineered Nanomaterials. Environmental Science and Pollution Research 2017, 24, 1553-1564.
- (89) Foroozandeh, P.; Aziz, A. A. Insight into Cellular Uptake and Intracellular Trafficking of Nanoparticles. Nanoscale Res. Lett. 2018,
- (90) Abakumov, M. A.; Semkina, A. S.; Skorikov, A. S.; Vishnevskiy, D. A.; Ivanova, A. V.; Mironova, E.; Davydova, G. A.; Majouga, A. G.; Chekhonin, V. P. Toxicity of Iron Oxide Nanoparticles: Size and Coating Effects. J. Biochem Mol. Toxicol 2018, 32, e22225.
- (91) Feng, Q.; Liu, Y.; Huang, J.; Chen, K.; Huang, J.; Xiao, K. Uptake, Distribution, Clearance, and Toxicity of Iron Oxide Nanoparticles with Different Sizes and Coatings. Sci. Rep 2018, 8, 2082.
- (92) Sukhanova, A.; Bozrova, S.; Sokolov, P.; Berestovoy, M.; Karaulov, A.; Nabiev, I. Dependence of Nanoparticle Toxicity on Their Physical and Chemical Properties. Nanoscale Res. Lett. 2018, 13, 44-44.
- (93) Tanimoto, A.; Kuribayashi, S. Application of Superparamagnetic Iron Oxide to Imaging of Hepatocellular Carcinoma. Eur. J. Radiol 2006, 58, 200-216.

□ Recommended by ACS

First Superferromagnetic Remanence Characterization and Scan Optimization for Super-Resolution Magnetic Particle **Imaging**

K. L. Barry Fung, Steven M. Conolly, et al.

FEBRUARY 23, 2023 NANO I FTTERS

RFAD 🗹

Improvement of Hyperthermia Properties of Iron Oxide **Nanoparticles by Surface Coating**

Marta Vassallo, Alessandra Manzin, et al.

JANUARY 04, 2023

ACS OMEGA

READ **C**

Nonmonotonic Superparamagnetic Behavior of the Ferritin Iron Core Revealed via Quantum Spin Relaxometry

Erin S. Grant, David A. Simpson, et al.

DECEMBER 19, 2022

ACS NANO

RFAD 17

pH Dependence of MRI Contrast in Magnetic Nanoparticle **Suspensions Demonstrates Inner-Sphere Relaxivity** Contributions and Reveals the Mechanism of Dissolution

Eoghan MacMahon and Dermot F. Brougham

FEBRUARY 03, 2023

LANGMUIR

RFAD 🗹

Get More Suggestions >